



HAL
open science

Lithospheric Strength and Rift Migration Controls on Synrift Stratigraphy and Breakup Unconformities at Rifted Margins: Examples From Numerical Models, the Atlantic and South China Sea Margins

M. Pérez-gussinyé, M. Andrés-martínez, M. Araújo, Y. Xin, J. Armitage, J. P Morgan

► To cite this version:

M. Pérez-gussinyé, M. Andrés-martínez, M. Araújo, Y. Xin, J. Armitage, et al.. Lithospheric Strength and Rift Migration Controls on Synrift Stratigraphy and Breakup Unconformities at Rifted Margins: Examples From Numerical Models, the Atlantic and South China Sea Margins. *Tectonics*, 2020, 39 (12), pp.e2020TC006255. 10.1029/2020TC006255 . hal-03114314

HAL Id: hal-03114314

<https://ifp.hal.science/hal-03114314v1>

Submitted on 18 Jan 2021

HAL is a multi-disciplinary open access archive for the deposit and dissemination of scientific research documents, whether they are published or not. The documents may come from teaching and research institutions in France or abroad, or from public or private research centers.

L'archive ouverte pluridisciplinaire **HAL**, est destinée au dépôt et à la diffusion de documents scientifiques de niveau recherche, publiés ou non, émanant des établissements d'enseignement et de recherche français ou étrangers, des laboratoires publics ou privés.



Distributed under a Creative Commons Attribution - NonCommercial 4.0 International License

Tectonics

RESEARCH ARTICLE

10.1029/2020TC006255

Key Points:

- Synrift stratigraphy closely mimics rift architecture, which depends on lithospheric strength and hence inheritance
- Basinward rift migration produces unconformities predating breakup and a breakup unconformity, BU, over the most outer margins
- Asymmetric margins present condensed synrift and a single BU in the narrow margin and before breakup migrating unconformities in the wide one

Supporting Information:

- Supporting Information S1
- Movie S1
- Movie S2
- Movie S3
- Movie S4
- Movie S5
- Movie S6
- Movie S7
- Movie S8
- Movie S9

Correspondence to:

M. Pérez-Gussinyé,
gussinye@uni-bremen.de

Citation:

Pérez-Gussinyé, M., Andrés-Martínez, M., Araújo, M., Xin, Y., Armitage, J., & Morgan, J. P. (2020). Lithospheric strength and rift migration controls on synrift stratigraphy and breakup unconformities at rifted margins: Examples from numerical models, the Atlantic and South China Sea margins. *Tectonics*, 39, e2020TC006255. <https://doi.org/10.1029/2020TC006255>

Received 17 APR 2020

Accepted 7 OCT 2020

Accepted article online 16 OCT 2020

©2020. The Authors.

This is an open access article under the terms of the Creative Commons Attribution-NonCommercial License, which permits use, distribution and reproduction in any medium, provided the original work is properly cited and is not used for commercial purposes.

Lithospheric Strength and Rift Migration Controls on Synrift Stratigraphy and Breakup Unconformities at Rifted Margins: Examples From Numerical Models, the Atlantic and South China Sea Margins

M. Pérez-Gussinyé¹ , M. Andrés-Martínez¹ , M. Araújo^{1,2}, Y. Xin^{1,3}, J. Armitage⁴, and J. P. Morgan⁵ 

¹MARUM—Center for Marine Environmental Sciences, University of Bremen, Bremen, Germany, ²CENPES Research Center, Petrobras, Rio de Janeiro, Brazil, ³Key Laboratory of Ocean and Marginal Sea Geology, Guangzhou Institute of Geochemistry, Chinese Academy of Sciences, Guangzhou, China, ⁴IFP Energies Nouvelles, Rueil-Malmaison, France, ⁵Department of Ocean Science and Engineering, SUSTech, Shenzhen, China

Abstract Synrift stratigraphy and the distribution of breakup-related erosional unconformities vary vastly between passive margins and cannot be explained by classical rifting models. Here we use numerical modeling to predict their spatiotemporal distribution. We show that synrift stratigraphy mimics rift architecture, which is controlled by lithospheric strength. Basinward rift migration during extension produces (1) oceanward younging, syntectonic and posttectonic sequences, (2) rift migration unconformities, RMUs, predating breakup, and (3) a breakup unconformity, BU, that only extends over the outermost margins, since breakup is not linked with a sudden stress drop. With small synrift sedimentation, the RMUs and BU laterally merge to form a margin-wide unconformity. In symmetric, wide conjugate margins, which arise for weak lithospheres such as the South China Sea, a long phase of distributed deformation with little subsidence results in early synrift sediment over most of the margins. RMUs merge into a single event that marks the subsequent focusing of deformation into a narrow breakup area, which experiences short-lived intense thinning and subsidence. In asymmetric conjugate margins, lateral rift migration transports shallowly deposited, early synrift sediments from the narrow to the wide, hyperextended margin, leading to a condensed syntectonic sequence and a single BU in the narrow margin and a series of RMUs in the wide one. For very weak lower crusts, lateral rift migration generates large synrift sag basins in the wide margin, as in Angola and Congo margins. Our models resemble the observed margins tectonic diversity and may be used as templates for interpreting their distal, unexplored areas.

1. Introduction

The preserved sedimentary record has been often used to constrain and map the tectonic evolution of basins and rifted margins, as sediments are more easily reached by drilling and imaged with seismic methods than their underlying crust and mantle. Sedimentary architecture and the tectonic evolution of the underlying lithosphere are linked by conceptual models of rifting that predict how sediment geometries develop during lithospheric extension. The pure shear model (by McKenzie, 1978) and models derived from it have deeply impregnated our interpretations of lithospheric extension, subsidence, and uplift during rifting. These models predict that sediments deposited before breakup, the synrift sedimentary units, should exhibit fan-like geometries, opening toward their bounding faults. Sedimentary units deposited after breakup should gently drape over previous topography, showing semihorizontal layering, indicative for thermal subsidence during the postrift phase. Synrift and postrift units have been assumed to be separated by an unconformity marking the age of breakup and start of seafloor spreading, the so-called breakup unconformity, BU (Falvey, 1974). However, in the last 30 yr, evidence from drilling, combined with higher-quality seismic data, has allowed us to infer that the age of sediments, and their geometry do not hold such a simple relationship to breakup age and deformation.

For example, along the northern Angola, Kwanza, and Congo basins, some seismic profiles show a wide, ~200 km, zone of hyperextended crust (i.e., crust less than 15 km thick), seaward of the necking zone,

overlain by a sag basin containing semihorizontal sedimentary units of synrift age (Contrucci et al., 2004; Karner & Gambôa, 2007; Moulin et al., 2005; Péron-Pinvidic et al., 2017; Unternehr et al., 2010). In northwestern Australia synrift aged units also exhibit a sag-like geometry (Driscoll & Karner, 1998). Karner and Gambôa (2007) note that all these margins exhibit large sag synrift sediment accumulations in places that are characterized by little faulting and shallow environments during rifting. Karner and Gambôa (2007) and Huismans and Beaumont (2011) have suggested that larger thinning of the lower crust (LC) and underlying lithosphere compared to the upper crust (UC) may generate little faulting, but large lithospheric thinning, allowing the deposition of sag sediments, that is, apparently unaffected by faults, during the synrift. Heat advected during lithospheric thinning may provide the anomalously low subsidence necessary to explain the shallow deposition of these sag, synrift sediments (Karner & Gambôa, 2007).

In addition, synrift erosional unconformities observed seaward of the necking zones and along the distal part of some margins have been suggested to result from relative uplift to shallower water depths or even the emergence above sea level of some portions of the margin in advanced stages of thinning (Chenin et al., 2019; Esedo et al., 2012). While magma-rich margins may be assumed to be regionally uplifted due to the thermal effect of an underlying plume, it has remained enigmatic why these relative uplifts should occur at non-magma-rich margins. The mechanisms that produce these unconformities cannot be explained by a McKenzie type model and may be intimately related to those producing the so-called BU. In its original definition, the BU is “the youngest cycle of subaerial erosion in a marginal basin which is very nearly the same age as the oldest oceanic crust in the adjacent deep ocean basin” (Falvey, 1974). Vintage seismic data from rifted margins offshore Alaska, Newfoundland, and the Northwest Shelf of Australia were used to expand this definition to include the pattern of sedimentation and subsidence at passive margins. In this sense the BU was defined as a regional event which marks the division between synrift sediments, with diverging bedding, to postrift, semihorizontal sediments deposited during the thermal subsidence phase (Couzens, 1992; Driscoll et al., 1995; Embry & Dixon, 1990). According to this definition tectonic subsidence should decrease in the sedimentary section above the unconformity (Reeve, 2017). It was also recognized that this stratigraphic timeline may vary in character, from a strong erosional unconformity on top of rotated fault blocks to a depositional conformity over grabens and half-grabens (Couzens, 1992). In some margins, where breakup occurred during a quiet magnetic period, the age of this unconformity has been used to date breakup. However, in other margins, the existence of such regional unconformities separating synrift and postrift strata has not been recognized. For example, in the northern sector of the West Iberia margin, the Deep Galicia margin, the so-called, “Aptian-Albian” breakup unconformity, is underlain by sag-like sediments in the proximal margin (IODP Sites 638 and 641); that is, it is posterior to the end of deformation in the proximal margin, while in more oceanward locations, it does mark the end of the synrift deformation over continental crust (IODP Site 640, Ranero & Pérez-Gussinyé, 2010). Other authors have inferred that the “Aptian-Albian” unconformity marks the end of mantle exhumation in a more oceanward position (Soares et al., 2012; Tucholke et al., 2007). Both interpretations indicate an oceanward migration in time and space of deformation. This migration is nowadays recognized in many margins and has been deduced from stratigraphic observations in the North Sea (Cowie et al., 2005; Walsh et al., 2003), Gulf of Corinth (Mattei et al., 2004), the Gulf of Suez (Gawthorpe et al., 2003), Alpine Tethys margins (Masini et al., 2013), the Mauleón-Arzacq basin (Western Pyrenees, Lescoutre et al., 2019), from fault and deformation kinematics in the West Iberia-Newfoundland margins (Pérez-Gussinyé & Ranero, 2005; Perón-Pinvidic et al., 2007; Ranero & Pérez-Gussinyé, 2010), and from numerical models of extension (Andrés-Martínez et al., 2019; Brune et al., 2014, 2017; Ros et al., 2017).

In this work we seek to understand the relationship between extensional processes and the stratigraphy of the sedimentary section. To this end, we use numerical models that couple lithospheric deformation to erosion and sediment transport processes. We analyze the distribution in space and time of syntectonic and posttectonic sequences, the development of major unconformities, and how they depend on the evolving strength of the underlying lithosphere. Note that we do not intend to perform an exhaustive study of the influence of the parameter space on sediment and margin architecture, as this was done in previous articles (Andrés-Martínez et al., 2019; Ros et al., 2017), but rather aim to show the general trends of this influence. We first shortly present the methodology, which is brief and mainly refers to Andrés-Martínez et al. (2019). Using our experience from previous parametric studies (Andrés-Martínez et al., 2019; Ros et al., 2017), we choose some representative models and discuss the mechanisms of unconformity formation at these

modeled margins. Subsequently, we compare our results to natural examples in the North Atlantic (Porcupine basin), the South Atlantic (Camamu-Gabon and Campos/Espirito Santo-Angola conjugates), and the South China Sea. In particular, we address the following questions: (1) How does lithospheric strength affect synrift sediment stratigraphy, including the formation of large synrift sag basins? (2) What is the spatio-temporal distribution of unconformities at margins, and what is their relationship with oceanward migration of deformation? And, finally, (3) what is the effect of breakup on formation of margin-wide unconformities?

2. Methods

The modeling results presented here are obtained with an improved version of the code presented in Andrés-Martínez et al. (2019), MILAMIN-Rifts, which is a Lagrangian code that stems from the MILAMIN finite element solvers (Dabrowski et al., 2008). MILAMIN-Rifts is a non-Newtonian viscoelastoplastic code that includes a Winkler bottom boundary condition, a free-surface, strain softening in the brittle and ductile domains, and which is coupled to a surface process solver. We model a 2-D section of the continental lithosphere and upper asthenosphere that is divided in three layers with different thermomechanical properties: the upper crust (UC), the lower crust (LC), and the mantle. Mantle includes an upper lithospheric mantle section consisting of dryer olivine and a deeper asthenospheric section, consisting of wetter olivine, separated by a 5 km transition zone. The model domain is subjected to half-extension velocities of 5 mm yr^{-1} on the sides to simulate far-field stretching. The initial model domain is 400 km long and 150 km deep. The resolution in the UC is of 1 km and of 5 km in the LC and mantle (supporting information Figure S1). Additionally, the interfaces between the UC and LC and the LC and mantle have a resolution of 1 km, so that the LC layer and the lithospheric mantle top has a higher resolution than 5 km at the UC to LC boundary and at the Moho (Figure S1). The main parameters for the models presented here are in Table S1, and their initial strength envelopes are shown in Figure S2. Table S1 lists additional parameters used in all models. See Andrés-Martínez et al. (2019) for the description of the mechanical and thermal solvers as well as the coupling between the tectonic model and the surface process models. Note that the time step for the mechanical and thermal solver is 10 kyr, whereas it is of 1 kyr for the surface process function. For the present study we used two types of weak seed to initialize deformation at the center of the model domain (Figures S3–S6): (1) a thermal weak seed located in the model center, TWS (also used in Andrés-Martínez et al., 2019), and (2) a random damage weak seed, RWS (see Figure S3). The RWS randomly weakens the lithosphere along an area of $>200 \text{ km}$ around the model center, with the weakening being more intense in the model center than in the sides (see the supporting information). This leads to deformation being distributed over a wider area at the model start than in models with a TWS (Figure S5). To set up the RWS we assign a random weakening in an area distributed along 100 km on each side of the model center. This is done by initializing a random value between 0 and 1 at each integration point in the model domain at the start of the model run. This random parameter is applied to the strain softening functions defined at each integration point, so that the friction angle or the preexponential factor in the viscosity at finite strain θ varies randomly across the integration points inside a given range (see the supporting information). This parameter is advected together with the mesh. The lower bound of this range is decreased in the center of the model following a Gaussian function, which in practice implies that the center of the model at the beginning of the time run is randomly mechanically damaged (Figures S4d and S5c). This approach is similar of the one described in Naliboff et al. (2017) with the differences that (1) we laterally attenuate the magnitude of the initial random damage instead of using a sharp transition and (2) every time that remeshing is required, a reinterpolation of the random field is done, instead of calculating a new random field. This means that we do not introduce new random weaknesses during the model run (as done in Naliboff et al., 2017).

In our models every material has its own phase (i.e., layer) so that material interfaces are also element interfaces. This avoids sharp property transitions inside the elements, which are to be avoided in Finite Element Modelling, FEM. The models presented here can handle discontinuous material phases; that is, oceanwards of the crustal breakup point crustal phases disappear and the top of the mantle in this area becomes the top surface. This is different to models in Andrés-Martínez et al. (2019) where we could only reduce the thickness of any phase to a minimum of 100 m. This new improvement reduces the number of remeshings,

especially after breakup, speeds up the experiments (reduces the number of elements), and also generates more realistic topographies in the areas where crustal breakup occurs.

As in Andrés-Martínez et al. (2019), we model the landscape evolution associated with surface processes based on the assumption that within the terrestrial domain there is always a supply of sediment to be transported (transport limited; see, e.g., Armitage, Whittaker, et al., 2018). This means that mass is transported downslopes as a function of the surface runoff and the local gradient. By conservation of mass this leads to a diffusion equation to solve for erosion and deposition (Smith & Bretherton, 1972). At the transition from the terrestrial to the marine domain runoff is assumed to no longer control sediment transport. In the marine domain it is assumed that wave and tidal energy transport sediment downslope. This is captured by switching the diffusion coefficient within the mass balance to one that decays with the depth of the sea floor (see Armitage, Burgess, et al., 2018; Kaufman et al., 1991). In order to reproduce hemipelagic deposits below sea level, we added a source term to the surface process model (see the supporting information), which was not included in Andrés-Martínez et al. (2019). This leads to more realistic offshore stratigraphy, especially in the distal margins where the influence of hemipelagic sedimentation is greater. In the postrift phase, we reduce the rate of hemipelagic sedimentation, since maintaining a constant rate of hemipelagic sedimentation throughout the model run would generate unrealistically thick postrift sequences (see Table S1 for sedimentation rates). A decrease in hemipelagic sedimentation in the postrift is observed in some margins (Cunha, 2008) and may be due to tectonic quiescence after breakup.

Note that at the extension velocities modeled here, magmatic production leads to the formation of a maximum of ~3 km thick of oceanic crust after breakup (see Figure 4 in Ros et al., 2017). Hence we are clearly within the realm of ultraslow spreading ridges, where mantle exposures and magmatic oceanic crust both occur (Dick et al., 2003). These domains are characterized by large offset faults indicative of stretching across a strong oceanic ridge axis (Dick et al., 2003). Hence, it is likely that the stress reduction due to magma injection at the model ridge after breakup is a second-order effect that will modulate the main stress field changes that we model here. One would need a 3-D model to properly simulate the effects of crustal magma injection, since stress concentrations linked to the lateral injection of weak dikes away from an axial volcanic center will lead, in 3-D, to enhanced axial stresses near the tips of the dike that cannot be accurately approximated in 2-D models. Instead, we imagine that the 2-D model is an approximation to the stress changes at timescales larger than those of an individual magma injection/freezing cycle, and the strengths modeled here reflect the average axial strength when averaged over many magma injection/freezing cycles.

3. Model Results

Our models show that the sedimentary architecture tends to mimic conjugate margin architecture; where conjugate margin architecture is asymmetric, sedimentary architecture is also asymmetric in terms of age and geometry, and the opposite is true for symmetric margins (Figure 1). Hence, to discuss the sedimentary architecture of margins, model results are presented in terms of conjugate margin tectonic architecture and lithospheric strength, since, as we will see, this also influences stratigraphic patterns. To produce these different architectural types we use different combinations of parameters (see Figures 1, S2, S4 and Table 1). These parameter choices are based on the well accepted notion that margin architecture depends on lithospheric strength, which reflects the integrated effects of (1) the geothermal gradient at the start of rifting, (2) the rheology and thus composition and thicknesses of crust and lithospheric mantle, and (3) the extension velocity (Brun, 1999; Brun & Beslier, 1996; Brune et al., 2017; Buck, 1991; Huismans & Beaumont, 2011; Nestola et al., 2015; Pérez-Gussinyé et al., 2001; Ros et al., 2017; Svartman Dias et al., 2015; Tetreault & Buitert, 2018, among others). In addition, the way that the model is initialized will influence the final margin geometry: a TWS located in the model center strongly weakens this area and tends to localize extension very quickly after the start of rifting (see Andrés-Martínez et al., 2019; Ros et al., 2017). This leads to more abrupt crustal thinning and narrower margins than when an RWS is used. For an RWS the initial weakening is subtler and distributed over a broader area, over a long period after rift onset; thus, margins become wider and present a less steep thinning profile (Figures S5b, S5c, S6b, and S6c; see also Naliboff et al., 2017).

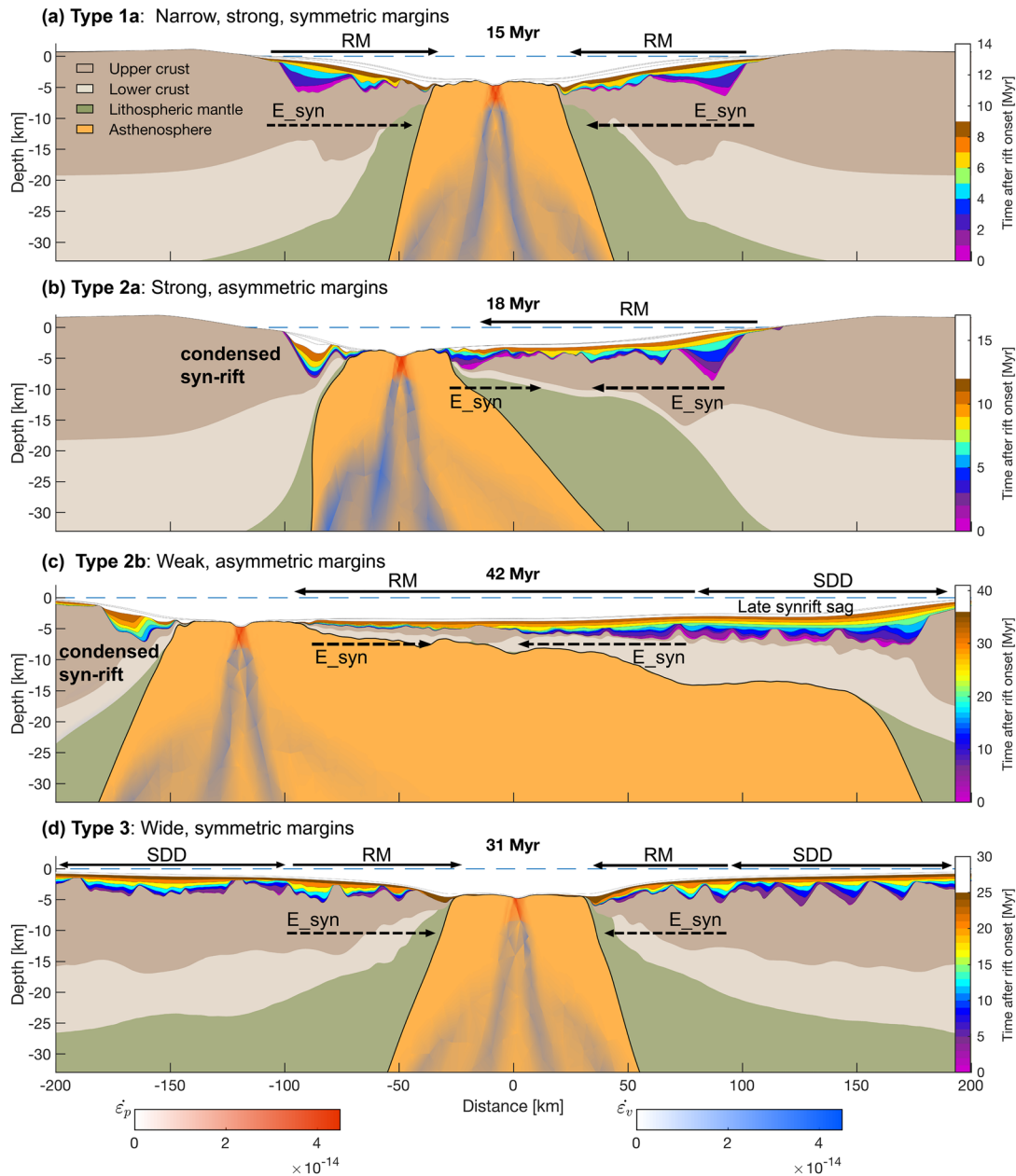


Figure 1. Snapshots of model evolution around 5 Myr after breakup for the main four different rheological profiles presented here (see Figure S1). See Table 1 summarizing the main characteristics and differences between the models. Half-extension velocity is 5 mm yr^{-1} in all models. Surface processes include pelagic sedimentation below sea level. Pelagic rate during the synrift, $\text{pesyn} = 0.3 \text{ mm yr}^{-1}$, unless otherwise stated, and in the postrift is 0.01 mm yr^{-1} . The decrease in pelagic rate in the postrift phase occurs within 5 Myr after breakup. Sediment age is shown in a rainbow color scale for the synrift and in white color for the postrift sediments. Brown sediments are those deposited just before breakup. Dashed blue line is the isostatically calculated sea level assuming that a 30 km thick crust is at sea level. Blue and red color scales and shading indicate plastic and ductile strain rate. (a) Type 1: narrow, symmetric margins: mafic granulite lower crust, 35 km crust. (b) Type 2a: strong, asymmetric margins: mafic granulite lower crust, 40 km crust. (c) Type 2b: weak asymmetric margins: wet quartzite and 40 km crust, $\text{pesyn} = 0.1 \text{ mm yr}^{-1}$. (d) Type 3: wide symmetric margins: wet anorthite and 35 km crust. Models (a) to (c) are initialized with a TWS, and model (d) is initialized with an RWS (see section 2). Unidirectional arrows show direction of rift migration, RM. Bidirectional arrows show areas of spatially distributed deformation, SDD. Dashed arrows, E_{syn} , show direction in which shallowly deposited early synrift sediment thins and often disappears. Domains characterized by SDD have comparatively thick and evenly distributed early, shallowly deposited synrift sediment. Symmetric RM displays early, shallowly deposited synrift thinning toward zero in the migration direction (see panel a). Asymmetric RM domains have a wide margin with a distal domain characterized first by thinning of shallowly deposited, early synrift sediment, until it disappears. This is followed by an oceanward outer domain where shallow early synrift reappears (panels b and c). This outer sequence has been laterally transported from the narrow margin towards the wide one. Consequently, the narrow margin presents a condensed synrift section with more proportion of late to early synrift than the wide margin proximal domain. The pattern of deposition of late synrift sediments on the wide margin depends on lithospheric strength: In weak margins, they form a sag basin over the SDD region and onlap on older sediments in the RM region.

Table 1
Models Described in the Paper, Their Main Characteristics, and Figures and Movies Where They Are Found

Model name	Architectural characteristics	Lower crustal rheology	Crustal thickness	Initial temp. at 35 km depth	Initial weak seed	Figures and movies
Type 1a: narrow, strong, symmetric margins	Narrow, symmetric margins, large offset faults, strongly rotated syntectonic sequences	Mafic granulite	35 km	600°C	TWS	Figures 1a, 2, 3, 10, 11, 12, S2, S4a, S7, and S8 and Movies S1, S7a, and S8a
Type 1b: narrow, weak, symmetric margins	Relatively narrow, symmetric margins, large offset faults, syntectonic sequences less strongly rotated	Wet quartzite	35 km	600°C	TWS	Figures S2 and S7 and Movie S2
Type 1c: narrow, intermediate strength, symmetric margins	Narrow, symmetric margins, large offset faults, strongly rotated syntectonic sequences	Wet anorthite	35 km	600°C	TWS	Figures S2, S5a, S6a, and S7
Type 2a: strong, asymmetric margins	Asymmetric margins, large offset faults	Mafic granulite	40 km	600°C	TWS	Figures 1b, 4, 5, S2, S4b, S9, and S10b and Movie S3
Type 2b: weak asymmetric margins	Asymmetric margins, small offset faults, one very wide conjugate margin	Wet quartzite	40 km	600°C	TWS	Figures 1c, 6, 7, 14, 15, S2, S4c, S9, and S10a and Movies S4, S5, S7c, and S8c
Type 2c: intermediate strength, asymmetric margins	Asymmetric margins, large offset faults	Wet anorthite	40 km	600°C	TWS	Figures 13, S2, and S9 and Movie S9
Type 3: wide symmetric margins	Symmetric margins, large offset faults, wide conjugates	Wet anorthite	35 km	700°C	RWS	Figures 1d, 8, 9, 16, S2, S4d, S5c, and S6c and Movies S6, S7d, and S8d

Note. The upper crustal rheology is wet quartzite, its thickness is 20 km, and its lithospheric thickness and basal temperature are 120 km and 1300°C, respectively, for all models. RWS refers to random weak seed, and TWS refers to random weak seed. Please see section 2 and the supporting information. Figure S2 shows the initial strength of these models. The rheological parameters and their references as well as other parameters used can be found in Table S1.

In all our models we have kept a constant mantle lithospheric composition and lithospheric thickness and the extension velocity at 5 mm yr⁻¹ half extension. We change lithospheric strength by changing (1) lower crustal rheology, (2) crustal thickness, (3) initial thermal profile, or (4) the initial weak seed. We present four main models in the results (Figures 1–9), Type 1a: narrow, strong, symmetric margins; Type 2a: strong, asymmetric margins; Type 2b: weak, asymmetric margins; and Type 3: wide, symmetric margins. For the discussion we use other intermediate rheologies that result in slight variations of the end-member rheologies presented in Figure 1 (see Table 1 and Figures S1–S10). The strength profiles and viscosities at the start of rifting for the models discussed are shown in Figures S2 and S4. Type 1a margins are produced with a mafic granulite rheology, the strongest lower crustal rheology used here, a 35 km thick crust, a temperature at the Moho of 600°C at the start of rifting, and a thermal weak seed, TWS (Figure 1a). Type 2a margins are produced by increasing the crustal thickness to 40 km and using the same rheology, geotherm, and a TWS as in the previous case (Figure 1b). A larger crustal thickness implies that the upper part of the strong mantle is “replaced” by weak LC, thus decreasing total lithospheric strength and leading to wider and in cases asymmetric margins (compare Figures 1a and 1b). A wet quartzite rheology, the weakest rheology used here, generates weak, asymmetric margins, that is, Type 2b margins, for the same geotherm, TWS, and crustal thickness as before (Figures 1c and S2). Finally, to generate very wide, symmetric margins, Type 3, we use a 35 km thick crust, with wet anorthite LC, a 700°C temperature in the Moho, and a random weak seed, RWS. Figures S5 and S6 show that for a model with wet anorthite and 35 km thick crust, increasing the temperature in the Moho from 600°C to 700°C and using a TWS result in an architectural change from narrow symmetric to asymmetric margins. Additionally, if the temperature at the Moho is kept at 700°C, but the initial weak seed is changed to an RWS, one obtains two wide symmetric margins where extension progresses very slowly until breakup.

In the following section we describe the results for the main architectural types shown in Figure 1. Why different modes of deformation occur with different initial rheological structures has been analyzed previously in Andrés-Martínez et al. (2019) and Ros et al. (2017). The relationship between melting, serpentinization,

and the final margin architecture was described in Ros et al. (2017), while the feedbacks between surface processes and lithospheric deformation were discussed in Andrés-Martínez et al. (2019). Below, we describe the models' evolution focusing on their implications for the geometry and age distribution of the sedimentary layers and on the development of unconformities. Note that to describe the structure of margins we distinguish between the proximal domain, where the crustal necking occurs, the distal domain, where the crust is hyperextended, that is, less than 15 km thick, and the outer domain, where the tectonic structures, that is, faults and shear zones, that led to final breakup are observed. In narrow margins, these domains overlap, so we distinguish only between proximal and distal/outer, where distal and outer are used to indicate the same area. Also, note that we differentiate between the terms synrift and postrift, which we adopt for sediment which was deposited before or after breakup time, irrespective of their geometries, from syntectonic and posttectonic. The latter terms refer to sediment that was deposited during or after tectonic activity in the underlying crust.

3.1. Type 1: Narrow, Symmetric Conjugate Margins

3.1.1. Type 1a: Strong LC Case

Figure 1a shows the margin and sedimentary architecture just after breakup and Figure 2a a zoom into the top part of the model and the depth trajectories of several markers in the basement. We assume that the simulated rifting event occurred in the geological past; thus, we use the adjective “younger,” for sediments whose deposition occurred later in the rifting history: Sediment deposited 20 Myr after rifting is younger than that deposited 5 Myr after rift start. Note that the strong LC in combination with an initial thermal weak seed, TWS, leads to strong spatial localization from the start of rifting and coupling of upper crustal and mantle deformation, so that faulting is accompanied by effective crustal thinning and rapid and symmetric breakup (Movie S1).

3.1.1.1. Evolution of Deformation

Movie S1 and Figure 3 show that deformation starts with two faults propagating into shear zones toward the initial TWS. These faults generate two initial half-grabens on either side of a central flexural bulge (Movie S1 and Figure 3a). The shallower position and geometrical configuration of the rift flanks leads to their erosion (Movie S1). With increasing sedimentation, the half-grabens deepen and, as a consequence, the curvature of the flexural bulge increases (1 to 3 Myr time steps in Movie S1). This results in the sediments deposited during the early phases of rifting being thicker in the half-grabens than on the flexural bulge (1 to 4 Myr in Movie S1 and Figure 3a).

As extension continues, the work needed to keep the main border faults active is larger than that needed to break new faults in the central flexural bulge, where strain is large due to its curvature. Hence new faults start to form in this central area (4 Myr onwards in Figure 3a and Movie S1). The main border faults become inactive at around 4 to 5 Myr, and faulting starts to dismember the central flexural bulge from then onwards (Figures 3b and 3c and Movie S1). Strong crustal thinning accompanies faulting. Final breakup occurs along a pair of conjugate seaward facing normal faults (F6 and its conjugate in Figures 2 and 3e). Their footwalls experience significant isostatic rebound (time steps 10–11 Myr in Movie S1 and Figures 2b, 3d, and 3e) that generates distal highs at the oceanward edge of both margins. With ongoing extension, the oceanic basement progressively rises to a shallower depth with respect to the subsiding distal margins (Figure 3f and Movie S1).

3.1.1.2. Syntectonic and Posttectonic Sediment Distribution

Several key observations stand out. First, the final conjugate margins are, overall, symmetric in terms of geometry and age of their sedimentary sequences (Figures 1a, 2, and 3 and Movie S1). Second, as the faults' life span is shorter than the total rift duration, each half-graben contains syntectonic sequences, which span a time interval shorter than the total rift duration, with overlying sag sequences that predate breakup. Third, due to basinward migration of the deformation, the top layer of the syntectonic sediment packages becomes younger oceanwards. The bottom of the posttectonic, sag-looking sediment packages also becomes younger oceanward; thus, the sag sequence thins oceanward (Figures 2 and 3). Additionally, the syntectonic sediment sequence dating from the first rifting phase (0–4 Myr in Figures 2a and 3) becomes thinner and almost disappears in the distal sections of the margins, as these areas represent the shallower parts of the initial central bulge, where this sequence was originally thinnest. Finally, due to progressive shallowing of the oceanic basement with respect to the subsiding distal margins, oceanward younging postrift sequences progressively onlap onto the oceanic basement (Figures 2a and 3f).

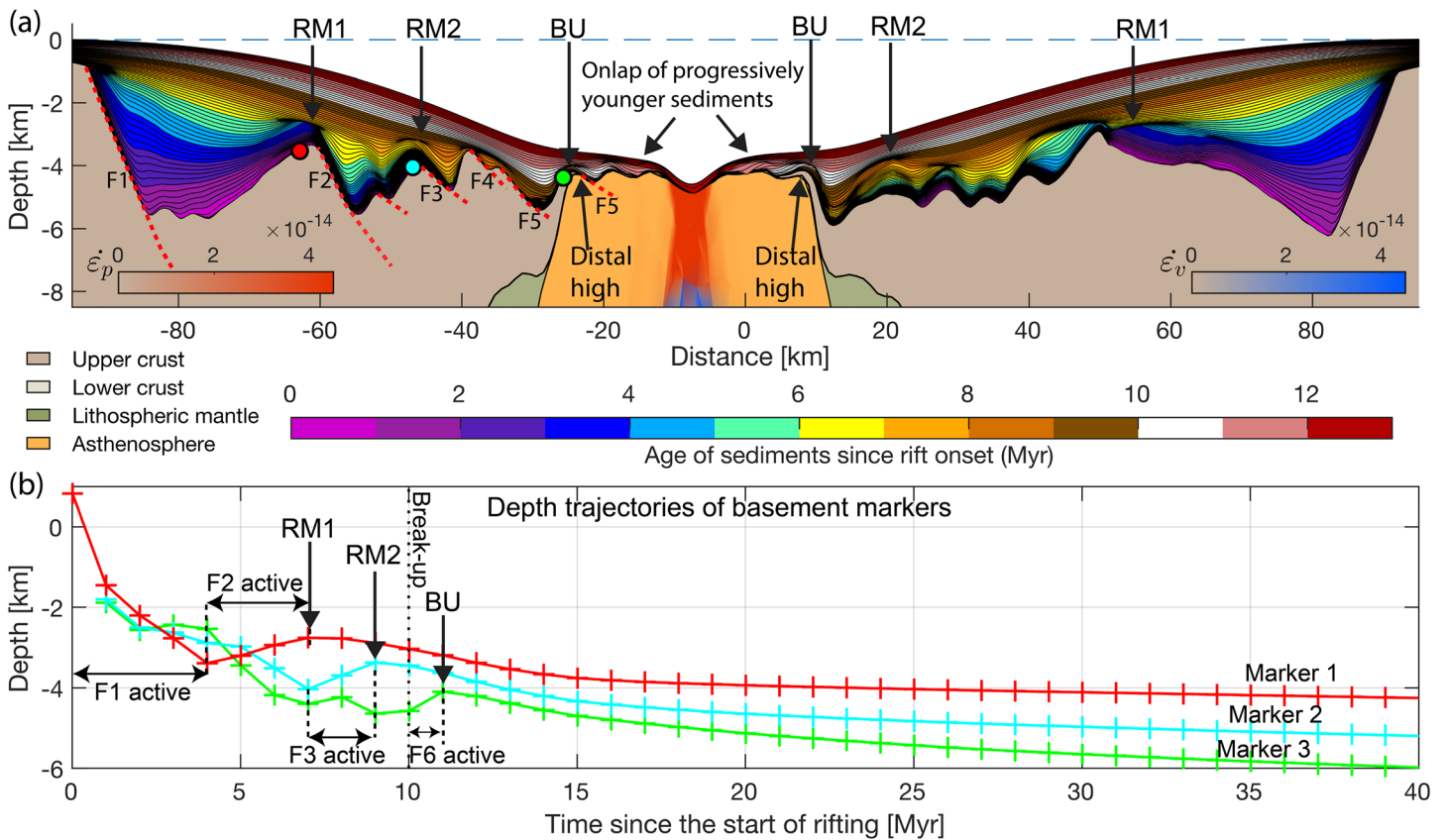


Figure 2. (a) Model Type 1a: narrow, strong, symmetric margins, at 13 Myr (Figure 1a and Table 1). Sediment age is shown in a rainbow color scale for the synrift and in white to red color scale for the postrift sediment. The dashed blue line is the isostatically calculated sea level assuming that a 30 km crust would be at sea level. Blue and red scales indicate plastic and ductile strain rate. (b) Depth of basement markers (shown in red, green, and cyan in panel a) during rift evolution. RM1 and RM2 are rift migrations unconformities, and BU is breakup unconformity. F1 to F6 are faults active during different times in rifting. Comparison of (a) and (b) shows that unconformities are formed when tectonic activity on large faults is abandoned and migrates oceanwards.

3.1.1.3. Development of Unconformities

As deformation migrates oceanward, each new faulting episode involves isostatic uplift and back rotation of the footwall blocks immediately landwards of active faults (Figure 2b). When these faults are abandoned the footwall blocks subside, resulting in the generation of angular and partly erosional unconformities at their crests. These unconformities mark the end of deformation on their oceanward bounding faults and the migration of fault activity, we call them “rift migration unconformities” (RM). Rift migration unconformities separate syntectonic from posttectonic sediment, which are both progressively younger toward the basin center and which predate breakup. In the models presented here we identify two RMs (RM1 and RM2 in Figures 2 and 3). The last of these episodes of flexural rebound at fault block scale corresponds to the breakup of the crust and the formation of new oceanic basement. Here, the sedimentary sequence, which onlaps the crest of the last distal basement high, forms an unconformity that postdates the breakup by 1 Myr, which is the time during which the distal high is formed (Figure 2b). We call this the “breakup unconformity” (BU) (Figures 2 and 3 and Movie S1). The sedimentary sequences deposited immediately landward of the distal high backrotate significantly as the oceanic basement rises in the model center (brown and first white units in Figures 2 and 3). We call these the “breakup sequences,” as they are syntectonic to the formation of the first oceanic crust or mantle exhumation (Figures 2 and 3).

3.1.2. Types 1b and 1c: Weaker LC Cases

Figure S7 shows the resulting configuration of two additional models that were run with increasingly weaker lower crustal rheologies (i.e., wet anorthite and wet quartzite). All models have a tectonic and sedimentary structure, which is fairly symmetric, with the exception of the wet quartzite one that presents a small degree of asymmetry in the most oceanward portion of the outer margin. In the proximal domains

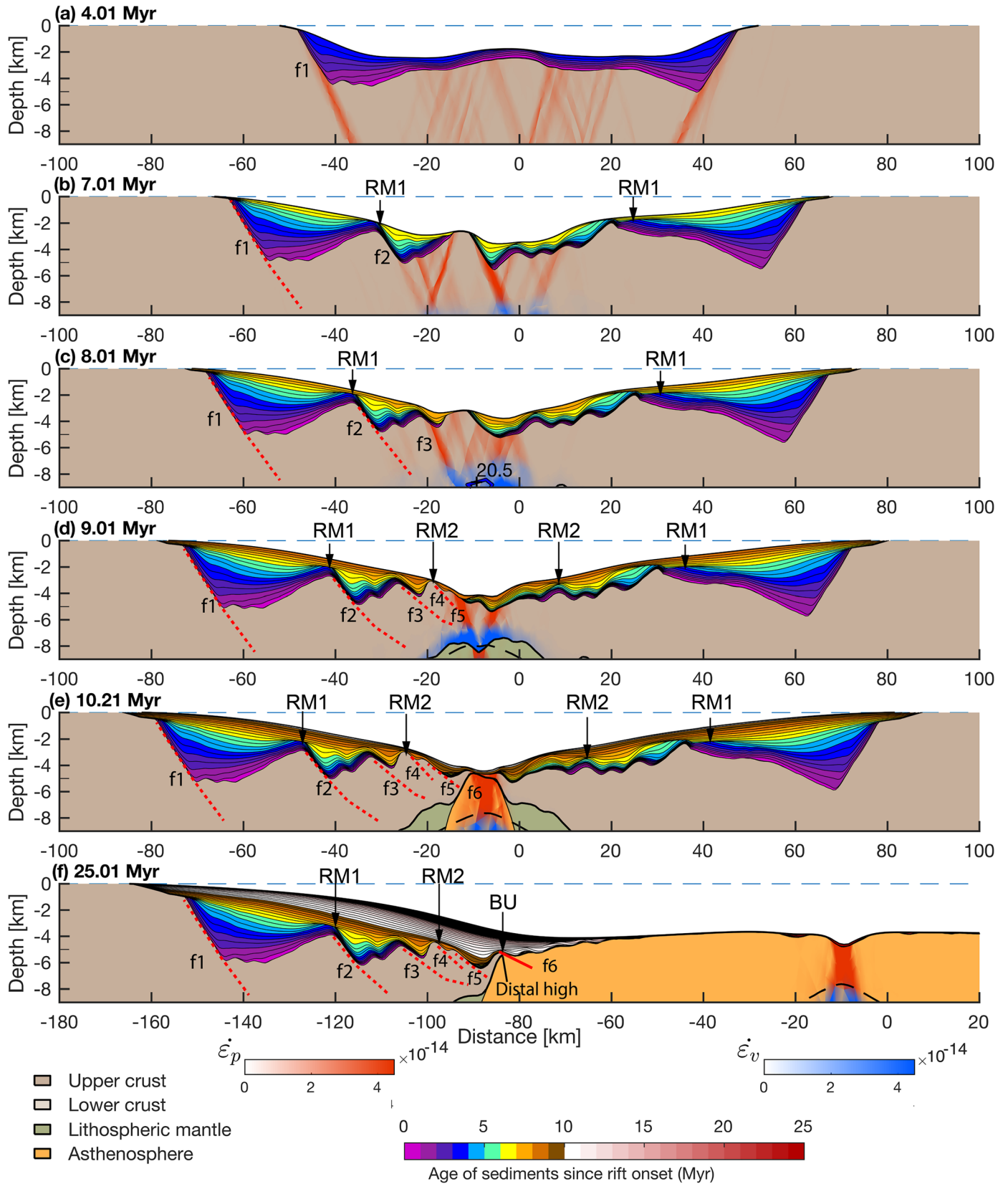


Figure 3. (a–f) Evolution in time of Model Type 1a: narrow, strong, symmetric margins (Figures 1a and 2 and Table 1). RM1 and RM2 are rift migration unconformities. BU is breakup unconformity. F1–F6 are main faults during margin development. Color scales as in Figure 2.

syntectonic sediments have less pronounced fan wedge-like geometries in the weakest case than in the stronger ones (Figure S7). In these areas, strong crust results in the generation of larger offset faults and thus larger block rotation during faulting. In addition, in the weak case, early syntectonic sediment (0 to ~5 Myr) is still largely present in the distal/outer margin. This is the result of a long phase of distributed deformation over a broad area in the first million years of extension in the weakest model (compare Movies S1 and S2). In the outer domain, the weak case presents a distal high, which is wide (Figure S7c, km -45 to -20), indicative of an increasing influence of ductile deformation in these areas compared to the distal parts of stronger models (Movie S2).

3.2. Type 2: Asymmetric Conjugate Margins

3.2.1. Type 2a: Strong LC Case

The resulting margin and sedimentary architectures are shown in Figures 1b, 4, and 5. The only difference between the models presented in Figures 4a and 4b is in the amount of synrift hemipelagic sedimentation, with 10^{-4} and $3 \times 10^{-4} \text{ m}^2 \text{ yr}^{-1}$, respectively. In Type 2a models, the crust is thicker by 5 km and consequently weaker, than in Type 1a model, so that crustal thinning is less efficient than in the previous case (Figures S2f, S4a, and S4b). This results in that breakup occurs later in the model run, and conjugate margins develop asymmetric structures, that is, a wide and a narrow margin.

3.2.1.1. Evolution of Deformation

As in the previous cases, deformation starts with two faults which propagate into two shear zones that point toward the initial TWS. These faults generate two initial half-grabens on either side of a central flexural bulge. The rift flanks erode and the grabens deepen with time, accumulating early synrift sediments (Figure 5a and Movie S3). From 5–6 Myr onwards deformation in the large rift bounding faults stops and moves into the central horst, where a series of faults that dip both oceanward and landward dismember it without being able to break it up (Figure 5b). These faults root into two shear zones that connect deformation from the UC to the mantle (Movie S3). With time one of these fault/shear zones accumulates more strain, weakens further, and becomes the focus of most of the deformation, promoting asymmetric upwelling of the asthenosphere and migration of rift activity toward its hanging wall (Figures 5c and 5d and Movie S3). This process repeats, leading to the formation of a system of oceanward younging sequential faults in the wide margin (see Ranero & Pérez-Gussinyé, 2010, for the kinematics, and Brune et al., 2014, and Ros et al., 2017, for the dynamics of this system). From 10 Myr onwards, faulting starts to cannibalize the initial half-graben located opposite to the migrating fault system (Figure 5c and Movie S3). This area will become the narrow margin after breakup. Lateral rift migration transports crustal blocks with early synrift sediment that was deposited in shallow conditions in the narrow margin to the future wide margin (Figures 5c–5e and Movie S3). The system of faults responsible for this lateral transport consists of a main deep-penetrating, oceanward dipping fault/shear zone located in the future wide margin (black dotted faults in Figure 5 and Movie S3) and a couple of shallower conjugate faults located in the future narrow margin. The deep-penetrating fault/shear zones transport deep crustal material, while the shallower conjugate faults transport the overlying sediments from the narrow to the wide margin. As a result, the final wide margin presents an outer domain characterized by very thin crust dissected by oceanward dipping faults/shear zones and a sedimentary section affected by landward dipping faults (Figure 5).

The narrow margin is characterized by abrupt crustal thinning and a deep half-graben, bounded oceanward by a distal high. This margin is formed by the dismemberment of the original crust and sedimentary section of the proximal half-graben, as it is transported to the wide margin.

3.2.1.2. Syntectonic and Posttectonic Sediment Distribution

The asymmetric evolution of deformation is reflected in an asymmetric distribution of sedimentary packages in terms of age and architecture. In the wide margin, the proximal domain consists of the half-graben that formed at the start of extension, which is located on top of the necking zone and which contains early synrift sediments that are syntectonic to the fault that bounds them (Figures 4 and 5). They are separated by an angular unconformity from the posttectonic, sag sediments. As deformation in this area stopped well before breakup, posttectonic/sag sediments have a younger age than breakup; that is, they are synrift. In the distal area, over the original central horst, which is underlain by 7–8 km thick crust, syntectonic and posttectonic sediments progressively young oceanwards reflecting the migration of rift activity toward one side of the rift (Figures 4 and 5g). The thickness of the syntectonic sediment package decreases over the dismembered central horst, as the early synrift was originally thinner there. Oceanwards, an area where basement has been

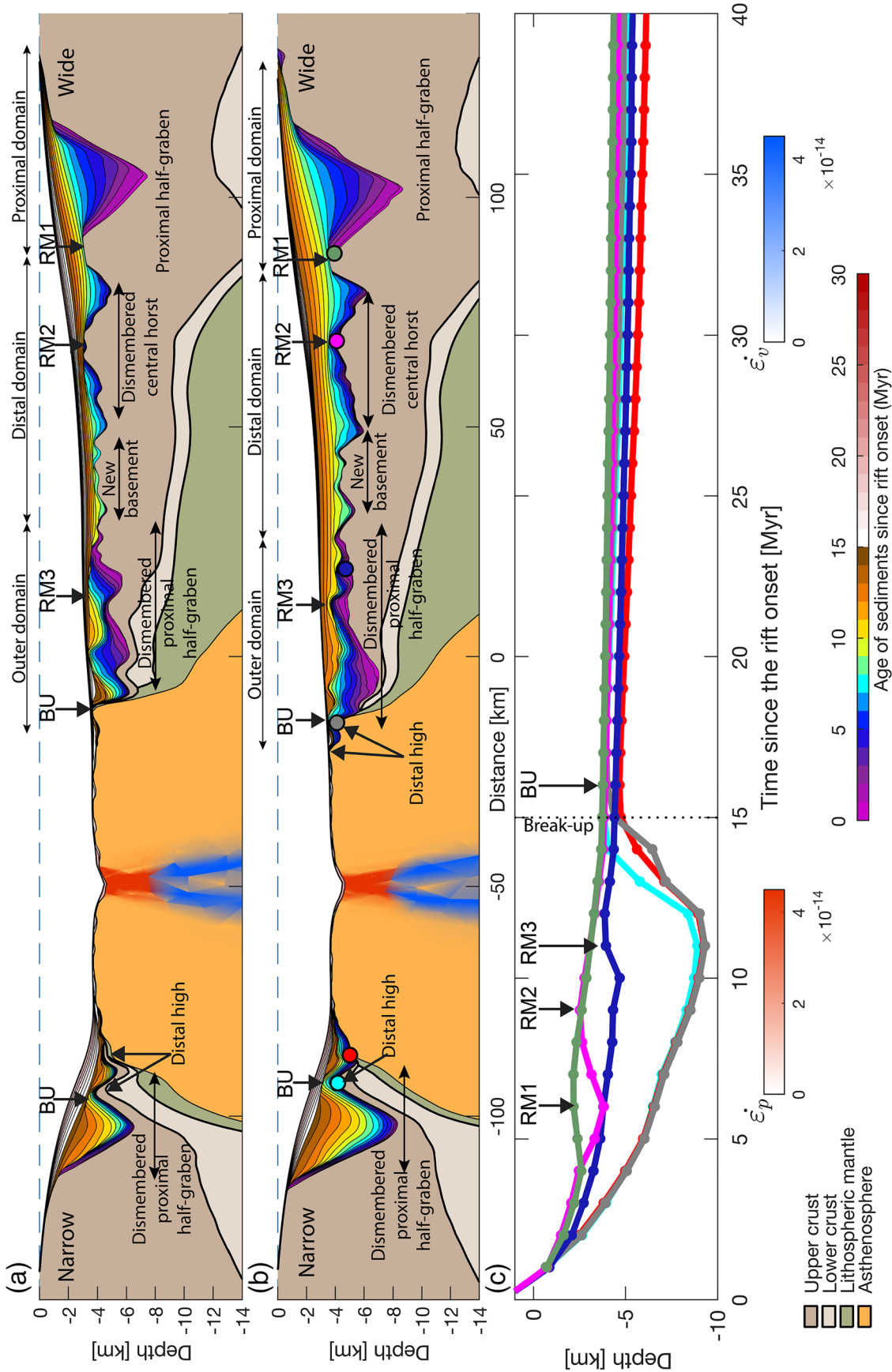


Figure 4. Model Type 2a: strong, asymmetric margins, at 20 Myr (Figure 1b and Table 1), with two different synrift pelagic sedimentation rates, $\text{pesyn} = 0.1 \text{ mm yr}^{-1}$ and (b) $\text{pesyn} = 0.3 \text{ mm yr}^{-1}$ (this is the same model as in Figure 1b). Sediment age is shown in a rainbow color scale for the synrift and in white to red color scale for the postrift sediment. Dashed blue line is the isostatically calculated sea level assuming a 30 km crust is at sea level. Red and blue shades are plastic and viscous strain rates, respectively. (c) Depth of basement markers during model evolution (shown in colored circles in panel b) during rift evolution. RM1 to RM3 are rift migrations unconformities, and BU is breakup unconformity.

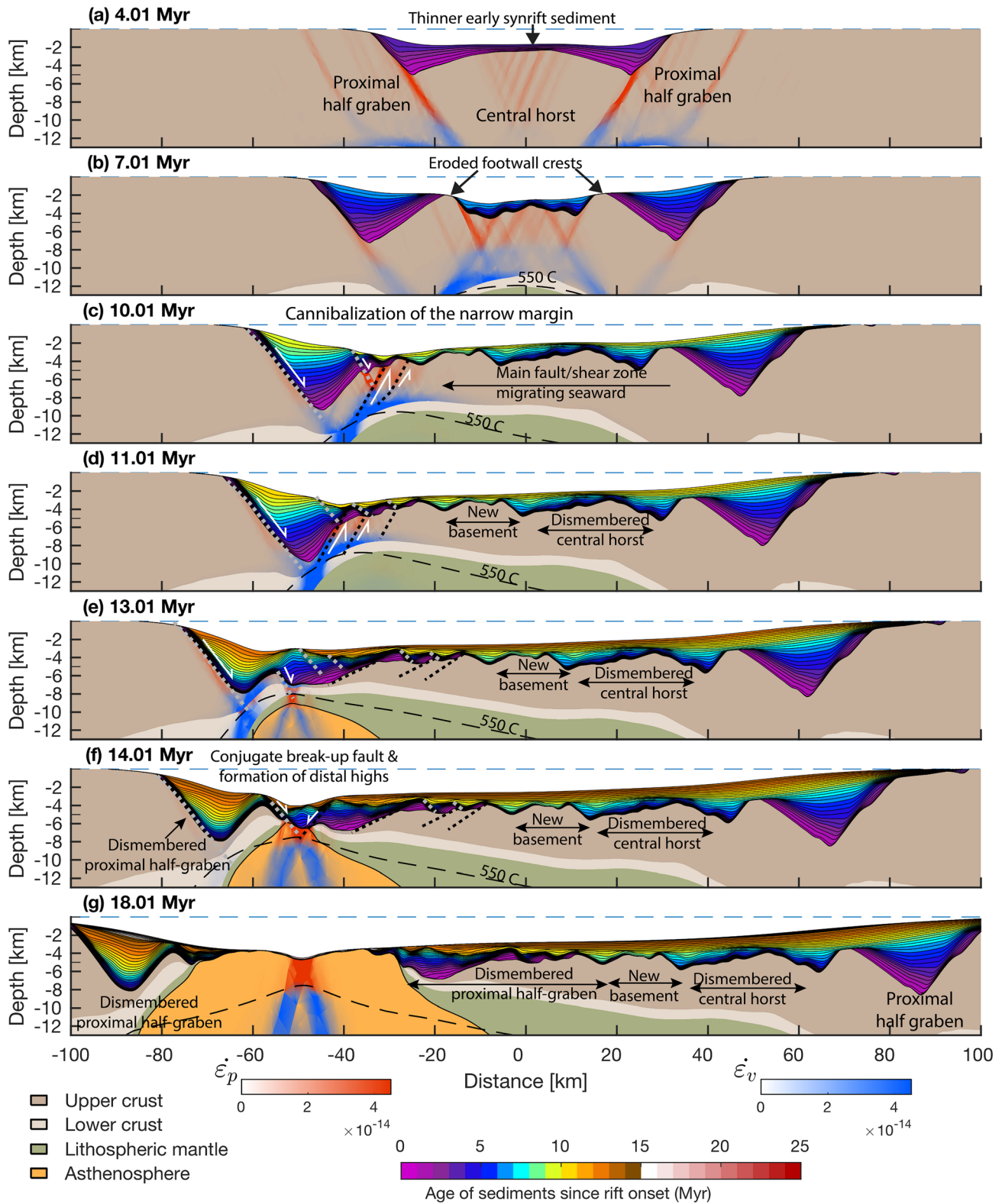


Figure 5. (a–g) Evolution in time of Model Type 2a: strong, asymmetric margins (Figures 1b and 4b and Table 1). Black dotted lines show oceanward faults located on the wide margin that affect the deep crust. Gray dotted lines show oceanward faults located in the narrow margin that affect the sedimentary section. White arrows show direction of displacement. Age of the sediment is shown in a rainbow color scale for the synrift and in white to red color scale for the postrift. The dashed blue line is the isostatically calculated sea level assuming that a 30 km crust would be at sea level. Red and blue shades show plastic and viscous strain rates, respectively.

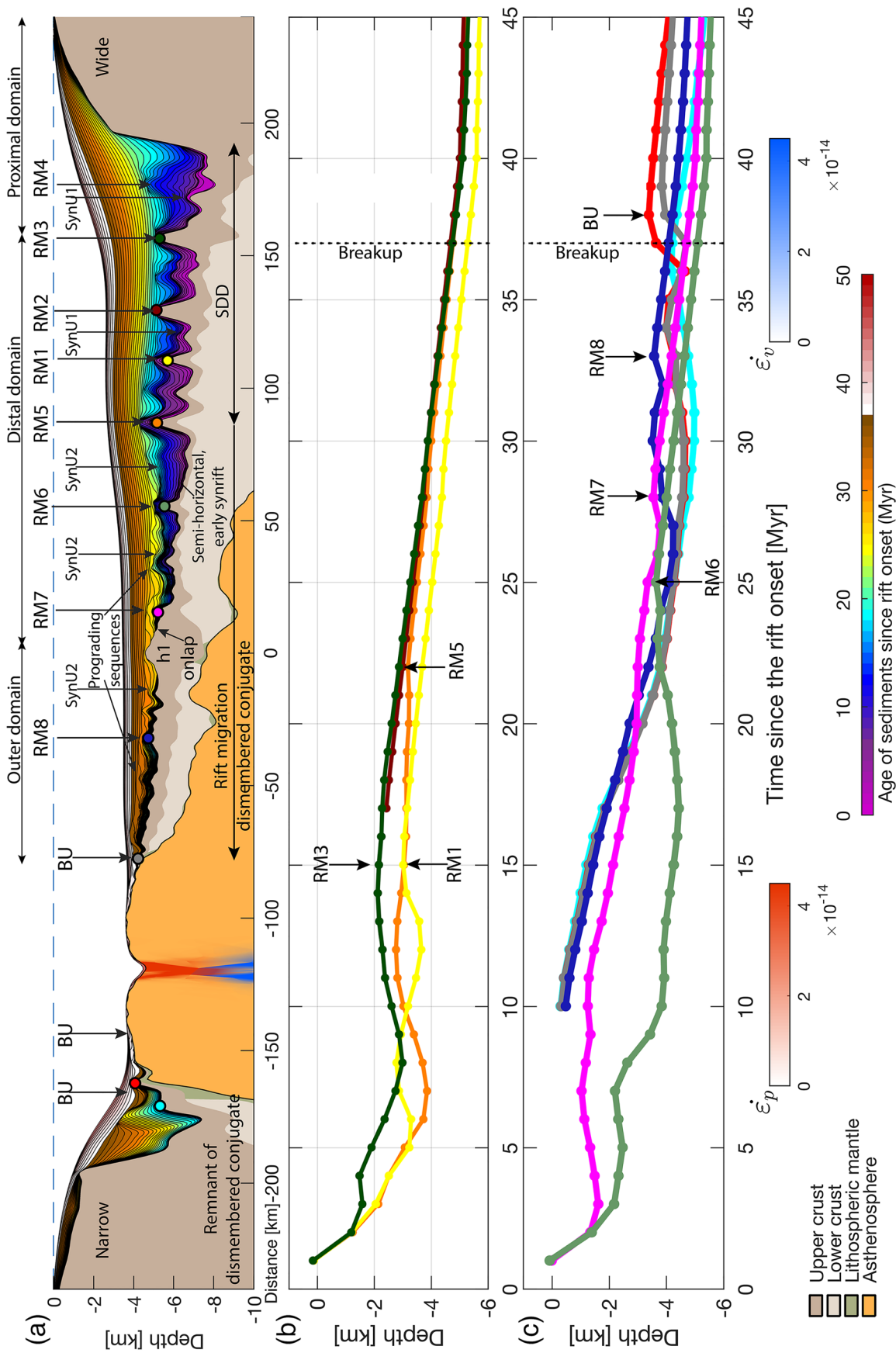


Figure 6. (a) Model Type 2b: weak, asymmetric margins, at 45 Myr (Figure 1c and Table 1). In the wide margin, SynU1 are angular unconformities within the syntectonic section during the initial phase of spatially distributed deformation. SDD is the area where this phase takes place. RM1 and RM5 are angular and erosional unconformities between syntectonic and posttectonic sections, formed as deformation is abandoned in one location and jumps to another one in the SDD. These unconformities are older in the center of the SDD than in the edges. RM5 is the last of these unconformities. From here onward deformation migrates laterally to the left of the model. SynU2 are unconformities within the syntectonic section that separate early syntectonic sediment from late syntectonic sediment. They form as the crust and sediments are transported from the future narrow to the wide margin. They are overlain by rift migration unconformities, RM6 to RM8. The last of these unconformities is the breakup unconformity, BU. Over the narrow margin there is only a single unconformity that marks the time of breakup, BU. h1 is the dismembered basement horst, which originally separated two half-grabens in the narrow margin. Panels (b) and (c) show the basement depths with time of the color tracers in (a). The times at which the unconformities are formed are indicated. Red dashed line marks breakup time.

exhumed from deep crustal levels and is overlain by younger sediment occurs, we call this the “new basement.” Here syntectonic sediments postdate the early rift phase (0–5 Myr, Figures 4a and 5g). In the outer domain, early synrift, syntectonic sediment deposited in rather shallow conditions overlies the hyperextended crust (purple to blue sediments, Figures 4 and 5g). The oceanward end of the outer domain of the wide margin is marked by a basement high that is the footwall of the last fault leading to crustal breakup. The syntectonic sediments here are extremely backrotated, and we call them the breakup sequences. The distal high is underlain by either extremely thinned crust or new ocean floor, before seafloor rises toward the shallower oceanic ridge (Figures 4 and 5).

In the narrow margin we observe a large proximal half-graben, which is the remnant of the original, now dismembered proximal half-graben. Because deformation is active in the narrow margin throughout the rift evolution, the syntectonic sediment age spans from early rift to breakup. Due to lateral transport of early synrift sediment from the narrow to the wide margin, the narrow margin contains a “condensed” synrift section, with much larger proportion of late synrift to early synrift sediments than the proximal parts of the wide margin. Posttectonic sediment in the narrow margin has an age postdating breakup (Figure 4). The oceanward edge of the margin is also marked by a distal basement high, which is the footwall to the last fault leading to breakup. At the outer domain of the margin early synrift sequences overly the first oceanic basement (Figures 4b and 5g). The narrow margin presents a thicker postrift sedimentary sequence than the distal and outer domains of the wide margin (Figure 4). This is because it exhibits a steeper bathymetric gradient than the wide one and is closer to the coast line. Finally, in both margins, the posttectonic and postrift sediments onlap onto the newly formed oceanic basement.

3.2.1.3. Development of Unconformities

The distribution of unconformities and their age is also quite asymmetric. In the wide margin a series of rift migration unconformities, RM1 to RM3, form as the footwall blocks backrotate and their crests erode during flexural uplift, and then subside due to fault activity abandonment with progressive oceanward migration of deformation (Figures 4c and 5 and Movie S3). Only the last of these unconformities, the BU, dates breakup. In models with little sedimentation (Figure 4a), these unconformities may be difficult to distinguish from each other and appear to laterally merge. They may therefore be misinterpreted as part of the same time line. In models where synrift sedimentation is larger (Figure 4b), sedimentary packages between the unconformities are thick enough to make unconformities clearly distinguishable from each other. In the narrow margin, since deformation is active throughout the whole rifting period, only one unconformity is observed along its whole length and it dates breakup; thus, all synrift sediments are syntectonic (see Figures 4 and 5 and Movie S3).

3.2.2. Type 2b: Weak LC Case

Figures 1c and 6 show the sedimentary architecture with the same sedimentation parameters as in Figure 4b, but with very weak wet quartzite LC. These conditions also lead to asymmetric conjugate margins, but the basement and sedimentary architecture is quite different to the previous models (Figures 6 and 7 and Movies S4 and S5).

3.2.2.1. Evolution of Deformation

Movies S4 and S5 and Figure 7 show the progressive thinning and spatial distribution of sediments with time. Because we have a TWS in the model center, deformation starts to be localized there. Two smallish half-grabens form at 2 Myr, but they are narrower and shallower than in the strong case (HG1L and HG1R, Movie S4 and Figure 7a). The very weak LC flows toward the areas of active upper crustal deformation to equilibrate lateral pressure gradients resulting from pressure lows at active faults tips, thereby preventing effective crustal thinning (lower crustal flow is shown by black arrows in Movies S4 and S5; Buck, 1991). With time lower crustal flow results in the distribution of deformation over a broad area, where faults dip both inward and outward, forming small grabens limited by local horsts. We call this the area of spatially distributed deformation (SDD, Figures 1, 6, and 7). By 18 Myr the width of the SDD is ~150 km (Movie S4) and deformation moves landwards of the limits of the initial half-grabens on both sides of the models, specially toward the left-hand side of the model, forming a graben landward of the initial one, which contains younger syntectonic sediments (proximal half-graben, HG2, Figure 7c and Movies S4 and S5). At 22 Myr, one of the fault/shear zones on one side of the SDD is favored and deformation starts to migrate laterally toward the left. As in the previous case, faults and shear zones cut into the future narrow margin, bringing sediments and deep crust from the narrow to the future wide margin. First, they bring the crust and

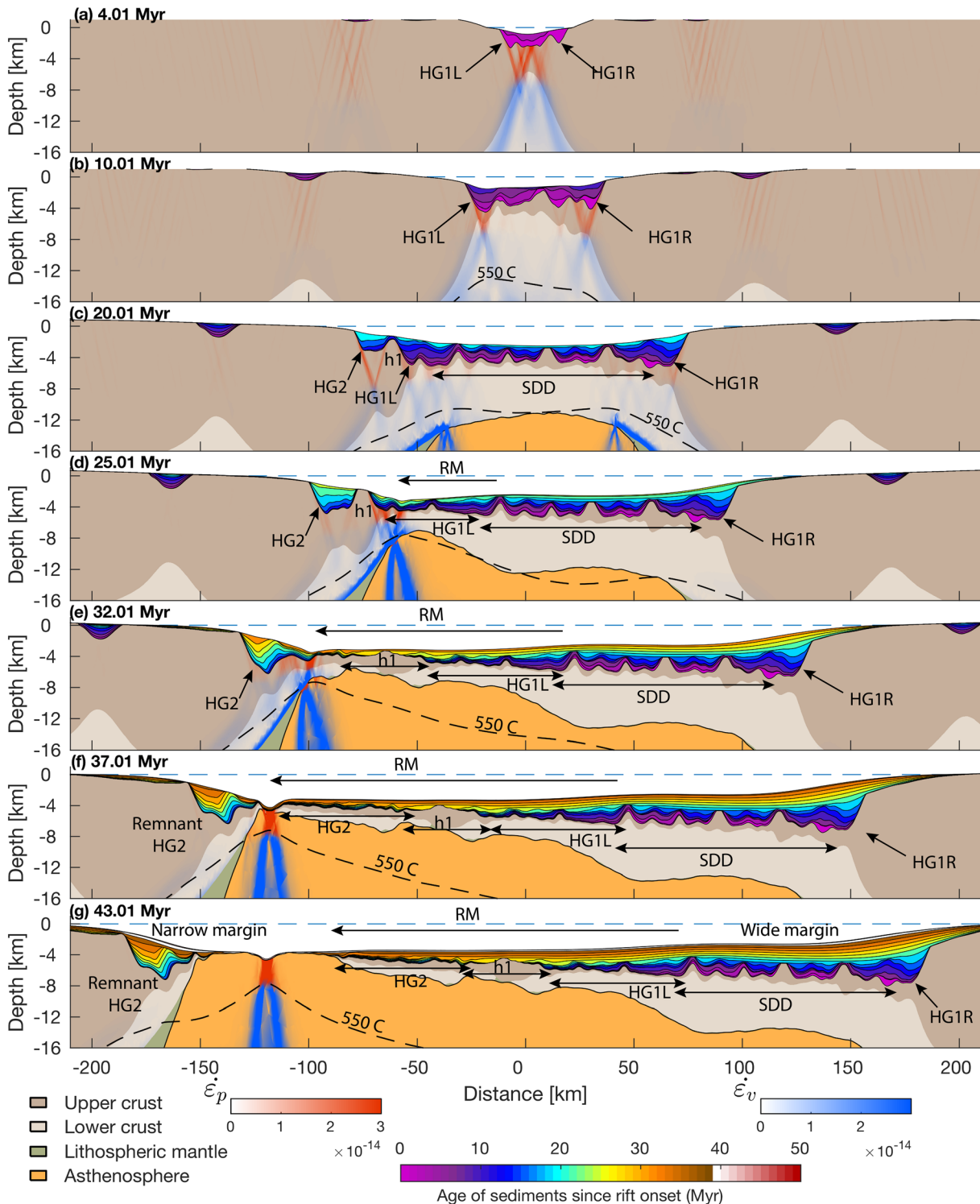


Figure 7. (a–g) Evolution in time of Model Type 2b: weak, asymmetric margins (Figures 1c and 6 and Table 1). SDD = central area of spatially distributed deformation; RM = area where rift migration occurs; HG1R and HG1L = proximal half-graben in left and right of model; HG2 = proximal half-graben formed at left of model at later time; h1 = horst separating HG1L and HG2. Crustal and sedimentary material from HG1L, h1, and HG2 are transported to the wide margin, where they constitute the distal and outer domains.

sediments from the proximal half-graben, HG1L, formed at the start of rifting; subsequently, they dissect the horst, h1 (which separated the half-grabens HG1L and HG2); and finally, they bring sediments and crust from HG2 toward the wide margin (Figures 7c–7e). Breakup occurs through a couple of oceanward facing conjugate faults, leaving two distal highs that delimit the narrow and wide margin.

3.2.2.2. Syntectonic and Posttectonic Sediment Distribution

The syntectonic and posttectonic sediment distribution is also asymmetric but quite different to the previous case. In the wide margin, the SDD area is characterized by small offset faults, forming horst and grabens, overlain by early synrift, syntectonic sediment, which exhibits less pronounced rotational geometries than in the strong case (Figures 6 and 7). Oceanwards of the SDD, the margin consists of rafts of crust and sediment that were transported from the narrow to the wide margin. This area is subdivided by a basement horst, the former h1 horst, which originally separated the two half-grabens in the narrow margin (HG1L and HG2, Figure 7). Landward of h1, the early synrift sediment is syntectonic to the formation of HG1L and pre-tectonic to the lateral transport of material. This sequence thins oceanward and presents a subhorizontal geometry, gently onlapping onto the landward dipping basement. Younger sediment is syntectonic to the lateral transport of material from the narrow to the wide margin and onlaps onto the older sediment forming progradational sequences (km ~20–80, Figures 6 and 7g). Basinwards, a basement high (i.e., former h1) is onlapped by progressively younger sediment. Further oceanwards, in the outer domain, the basement is composed by crustal rafts of the most landward half-graben of the narrow margin (HG2, Figures 6 and 7). Because HG2 formed later during the rifting history than HG1L, the sediments overlying the basement landward of h1 are older than those overlying the basement oceanwards of h1 (Figure 6). These sediments are onlapped by later synrift sediment, which is syntectonic to the lateral transport of HG2 into the wide margin and also portray a progradational geometry. Note that some of the sediments affected by lateral rift migration that sit on top of the hyperextended crust on the wide margin were at shallower depths for long time over the rift history (pink, blue, and gray markers, Figure 6c) than were more proximal sediments (yellow, orange, and dark green markers, Figure 6b). Classical models of rifting would suggest that this observation would indicate that the hyperextended crust was at a shallower depth than expected, due to an excess of lower crustal and mantle thinning with respect to upper crustal thinning. Instead, in our model, this arrangement arises from the lateral transport of sediment from the narrow to the wide margin, not to a “subsidence deficit.” Furthermore, note that the whole wide margin is capped by a synrift sag basin that thins and whose bottom age youngs oceanwards.

The narrow margin is the remnant of the most landward half-graben located in the narrow margin, HG2. It contains syntectonic sequences that date the age of its formation, which postdates the start of rifting, up to sequences with a breakup age. Because some of the earliest synrift sediment has been transported into the wide margin, the narrow margin presents a “condensed” stratigraphic section. Syntectonic sediment geometry appears to indicate a larger proportion of ductile deformation in the crust than in the strong mafic granulite case. Finally, because this margin is narrow, it is closer to the sediment source, so that the postrift sequence is thicker here than in the distal part of the wide margin (Figures 6 and 7).

3.2.2.3. Development of Unconformities

The formation of unconformities in this model reflects the distinct phases of crustal deformation, including an initial phase of spatially distributed deformation over a wide area, SDD, and a final phase of lateral migration of deformation that leads to breakup. The SDD produces angular unconformities within the syntectonic section, as faults move within a broad central area from one location to the other, tilting the syntectonic sediments in opposite directions. We name these syntectonic unconformities of the first deformation phase, SynU1 (km ~80 to ~200, Figure 6 and Movie S4). This initial SDD also produces erosional unconformities at higher levels within the sedimentary section that cap the crests of footwall blocks. These unconformities separate syntectonic from posttectonic sediment and are formed as deformation at a given fault block is abandoned and moves elsewhere. They are older in the center of the SDD area, and younger toward its edges, reflecting the migration of deformation from the center toward the edges (Figure 7 and Movie S4). We name these rift migration unconformities (RM) and number them according to their age from older, RM1, to younger, RM5. The youngest of these unconformities is at the oceanward edge of the SDD area, RM5 (Figures 6 and 7). From here oceanwards the margin is formed by crust and sediments that have been transported from the narrow to the wide margin. Thus here we also find unconformities within the syntectonic section that separate original syntectonic sediments that were deposited during early synrift in the

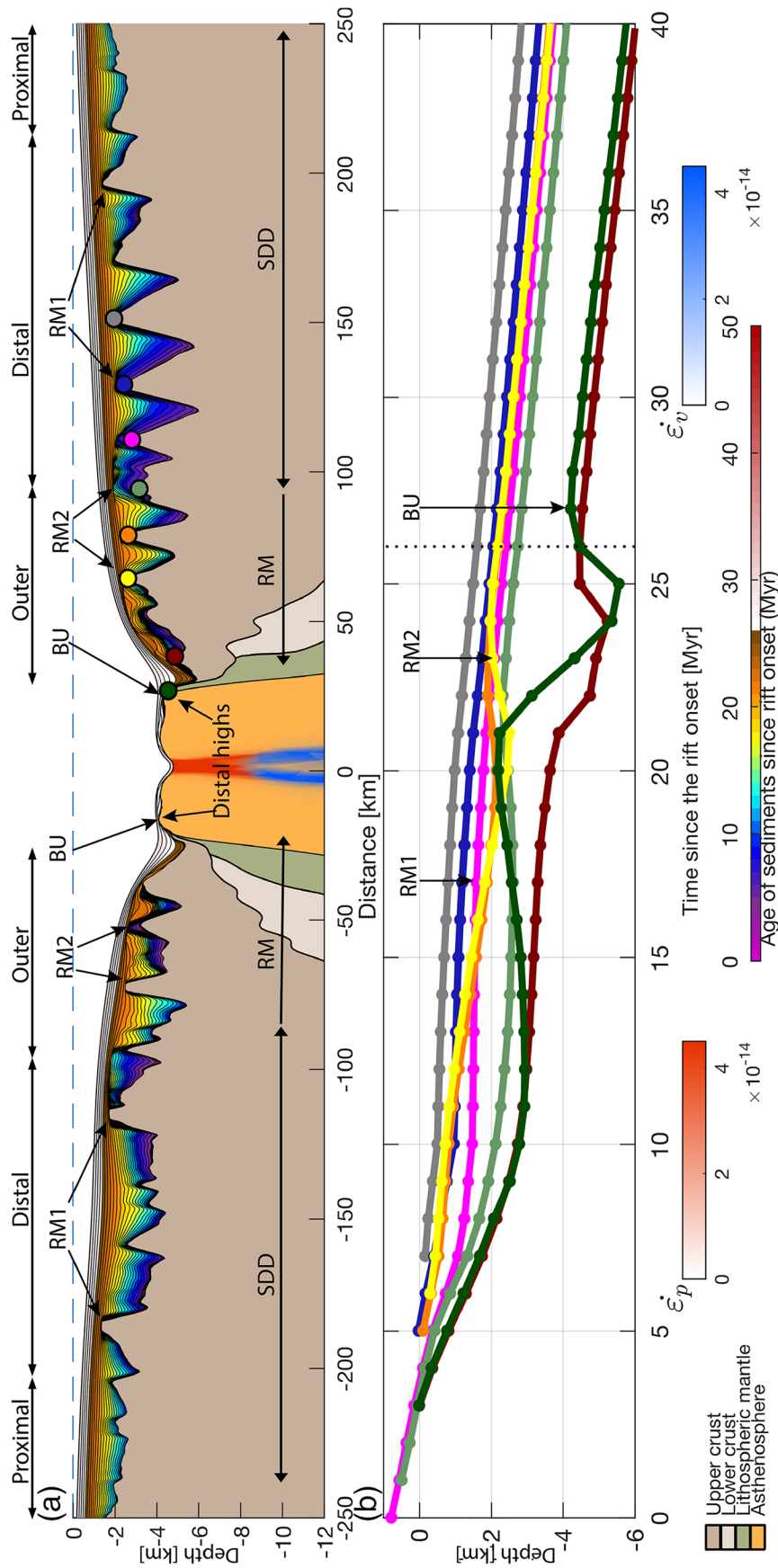


Figure 8. (a) Model Type 3: wide, symmetric margins (Figure 1d and Table 1). The deformation here starts with a very long phase of spatially distributed deformation (SDD), which lasts for around 20 Myr, followed by a short phase, 5 Myr long, of strong localization and oceanward rift migration, RM, in a relatively narrow area where breakup finally occurs. RM1 are unconformities which mark the end of the phase of the SDD. RM2 are unconformities marking the start of the localization and rift migration phase, and BU is the breakup unconformity. Panel (b) shows the basement depths with model evolution of the color tracers in (a). The times at which the unconformities are formed is indicated. Red dashed line marks breakup time. In both cases blue dashed lines mark sea level. Note that in (b) vertical coordinates have been shifted so that sea level is at zero, while in (a), 0 depth is the top of the model at the start of rifting. The blue line in (b) marks the depth of markers in (a) at the time of 30 Myr.

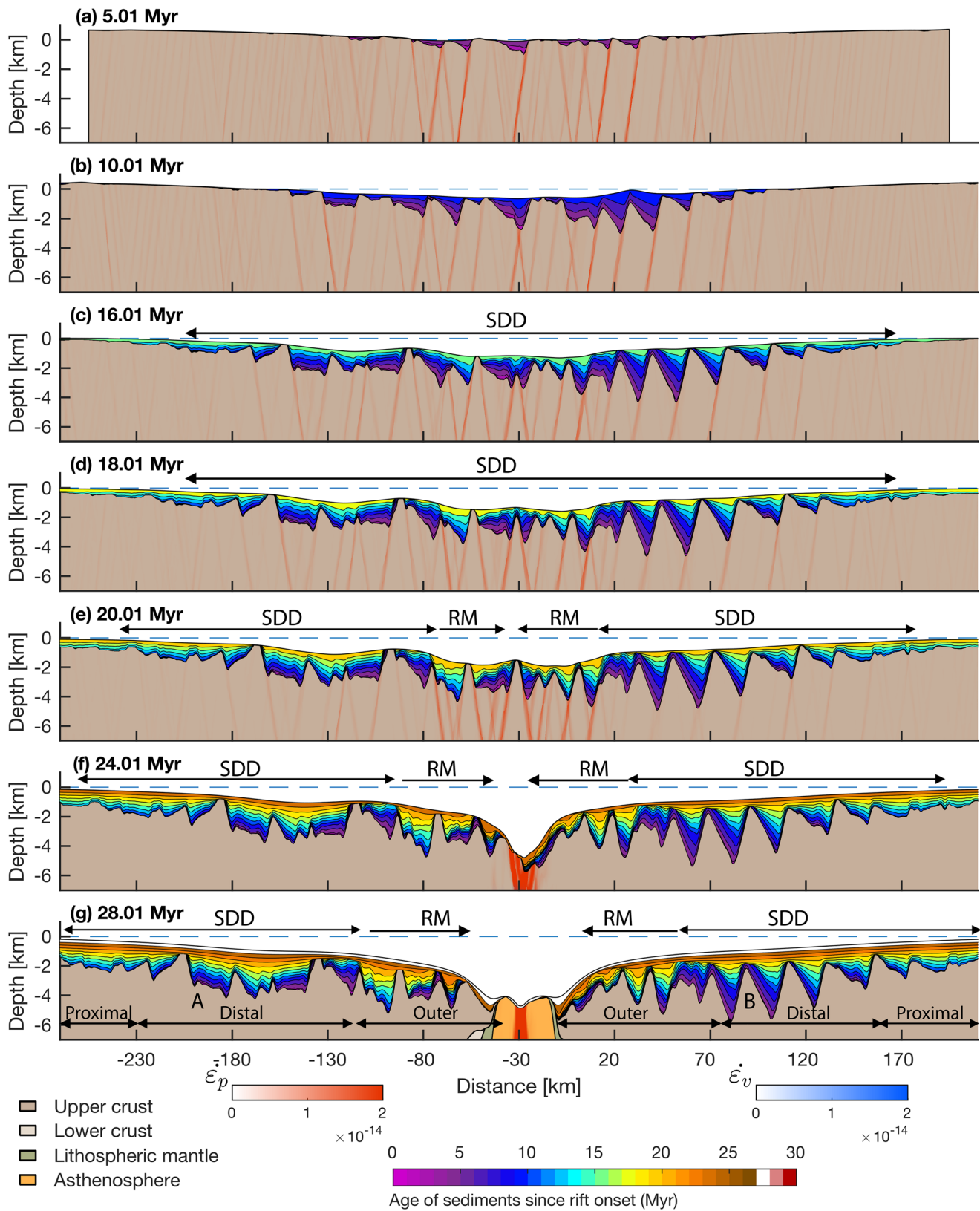


Figure 9. (a–g) Evolution in time of Model Type 3: wide, symmetric margins (Figures 1d and 8 and Table 1). SDD = central area of spatially distributed deformation; RM = area where rift migration occurs. Dashed blue line is sea level. Sediments are color coded according to age. Blue and red color scales show plastic and ductile strain rate.

narrow margin, from syntectonic sediments that were deposited during the lateral transport from the narrow toward the wide margin, these are here named SynU2 (Figure 6). These syntectonic sediments are separated from sag-looking, posttectonic, synrift sediments by unconformities that date the oceanward migration of deformation, RM6 to RM8, and separate an oceanward progressively younger sedimentary sequence both below and above the unconformity. The last of these unconformities dates breakup, and we name it the breakup unconformity (BU). As in the strong case, in the narrow margin, we find only one unconformity, which dates breakup, the BU (Figure 6).

3.3. Type 3: Wide, Symmetric Conjugate Margins

Wide symmetric margins are generated by a model with wet anorthite rheology in the LC and with a higher geothermal gradient than in previous models (Figure S2). In addition, this model is initialized with a random weak seed, RWS (see section 2 and the supporting information). The effect of the higher temperature Moho is to decrease the viscosity of the LC and subcrustal lithospheric mantle. This, in combination with the RWS, inhibits strong localization during most of the model run, so that crustal and lithospheric thinning occur slower than in models with the same rheology and temperature but a TWS (Figures S5 and S6). These initial conditions result in the formation of symmetric margins, which thin very gradually over a broad area (Figures 1d, 8, and 9 and Movie S6).

3.3.1. Evolution of Deformation

The deformation in this model is widely distributed for a long time since the start of rifting, forming horsts and grabens over an area of around 200 km on each side of the model center (Figures 9a–9d and Movie S6). Subsidence of the basin occurs slowly over this area (Figure 8b). About 20 Myr after the start of rifting, deformation localizes in the center of the model in a series of faults, facing both inward and outward of the basin. These faults are coupled to shear zones in the LC and mantle, producing effective crustal thinning and rapid subsidence (green and dark red markers Figures 8 and 9 and Movie S6). Breakup occurs along two conjugate faults at the model center at 26 Myr. After breakup the ocean floor isostatically rises and backrotates the syntectonic sedimentary sequences deposited during breakup.

3.3.2. Syntectonic and Posttectonic Sediment Distribution

Here, sedimentary architecture is symmetric on both conjugate margins. Because of the long period of spatially distributed deformation, in the SDD area, syntectonic sediments of age 0–20 Myr are found over most of the basin, over 200 km on each side of the basin center, in the distal and outer domains. Additionally, the LC is not as weak as in the previous example (Figures 1 and S2), and clearly defined syntectonic rotational wedges can be observed. At 20 Myr deformation localizes in a narrow area in the basin center. Thus sediment of 20 to 26 Myr in age is posttectonic over the SDD and syntectonic over the final breakup area (Figures 8 and 9).

3.3.3. Development of Unconformities

The unconformities are symmetric on both conjugate margins (Figure 8). In the proximal margins, there is so little faulting that no clear unconformity can be followed, instead the change from syntectonic to posttectonic sediments is very gradual, without evidence for angular or erosional unconformities. In the distal domains, unconformities are located on the faulted blocks crests and separate syntectonic from posttectonic sequences, both of which are synrift. These unconformities are almost synchronous and mark the time, ~17–20 Myr, when deformation focused in the model center and led to rapid thinning and breakup (see unconformities RM1). The outer area is affected by the final deformation that led to rapid thinning and breakup after 20 Myr, and unconformities there separate syntectonic from posttectonic sediment, both of which become progressively younger oceanwards (RM2, Figure 8a). These unconformities form during footwall block rotation as deformation moves progressively oceanward. The last of these unconformities is the breakup one, which separates sediment that was syntectonic with the formation of the distal highs on both margins, from posttectonic sediments (Figure 8). The BU postdates breakup by around ~1 Myr, as the distal high continues to form after the crust has broken up. The sediments deposited during the formation of the distal highs are strongly backrotated, and we call them the breakup sequences.

4. Discussion

The models presented previously allow us to discuss the imprint of breakup on the stratigraphic record and how our modeled margin geometries can be used to understand stratigraphic patterns in seismic sections in various margins of the world.

4.1. Formation of Unconformities and Distal Highs: Does Breakup Lead to a Margin-Wide Unconformity?

The origin of vertical movements of uplift and subsidence that generate unconformities at margins and how they are related to the breakup event has been much discussed in the literature. Falvey (1974) suggested a conceptual model in which extensive vertical uplift during breakup and associated asthenospheric upwelling would cause significant erosion throughout the basin and the formation of a BU dating the onset of sea-floor spreading. He noted that this unconformity was usually localized over the rift shoulders at the basin flanks and high blocks. This unconformity should separate synrift sediments affected by faulting from post-rift sediments, which should be undeformed. The later pure shear model (Mckenzie, 1978) could provide a quantitative description of the subsidence and uplift during rifting but could not explain the occurrence of either the BU or the observation of rift flanks that border the margins. Subsequent mechanisms proposed to explain the formation of breakup unconformities aimed to also explain observed rift flank uplifts. Proposed rift shoulder uplift mechanisms included lateral heat conduction outward of the basin (Cochran, 1983), depth-dependent stretching (Royden & Keen, 1980), small-scale mantle convection (Keen, 1985), and regional isostatic compensation of a thinning lithosphere with intrinsic strength (Braun & Beaumont, 1989). All those mechanisms probably operate to some degree during extension; that is, the thinning of the mantle occurs over a larger wavelength than the crust, even in cases where extension may be considered to be uniform with depth. However, there is now consensus that the intrinsic strength of the lithosphere is probably the most dominant factor that contributes to uplift of the rift shoulders and vertical movements that lead to unconformity formation (see also Weissel & Karner, 1989). Braun and Beaumont (1989) noted that at the rift flanks, the BU merges with others to form an amalgamation of unconformities and that sediments from the sequence above the unconformity young landward. This was interpreted as an indication for uplift of the rift shoulders during rifting and subsequent subsidence and erosion during the post breakup period. They suggested that rifting and necking of a strong lithosphere (with a depth of necking deeper than the Airy compensated depth) is what controls vertical movements in the basin. This generates basin overdeeps (areas where the basement depth is larger than the Airy basement), and permanent rift flanks, which could only be later removed by erosion. After lithospheric rupture, the continuous in-plane stress along the rift zone would not be longer sustained, so that it would drop to zero at breakup. They used a finite element grid that was extended up to an extension factor of 4.5 and then artificially dropped the horizontal stress to zero to simulate lithospheric rupture. They found that this led to a deepening of ~200 m of the previously formed rift flanks and a corresponding shallowing of the distal parts of the margin. They hypothesized that the shallowing in the basin would create an apparent decrease in sea level and a BU.

In this work, we also find that breakup results in a shallowing of the basin center and a deepening of rift flanks (Figure 10). However, there are important differences when compared to the findings of Braun and Beaumont (1989). First, we find that the deepening of the rift flanks is a continuous process that occurs when the main rift faults become abandoned and deformation moves basinward (see Figure S8 and Movie S1). Importantly, the uplift of the rift center in response to breakup is not a basin-wide phenomena. Instead, it actually occurs within a laterally constrained region, at the fault block scale, and it only affects the footwalls of the last faults that lead to breakup (Figure 10). This uplift produces the distal highs that are observed at so many margins, and a local unconformity over the distal high, which we have named the breakup unconformity, BU (Figure 10).

After breakup the new ocean floor continues to uplift, while the margins subside (Movies S1–S4 and Figures 10c and 10f). After 30 Myr of model evolution, the ocean floor rises to a shallower position in the model with surface processes, as sediment loads push the distal and outer margins down and the new ocean floor bends in response to this evolving surface load (Figures 10d). This shows that the post breakup margins and the new oceanic lithosphere continue to be welded in this model. Indeed, Figure 11 and Movie S8 show that at breakup and for some time thereafter horizontal stress stresses remain nonzero and similar within the lithospheric mantle beneath the distal margins and the mantle beneath the new ocean floor. Thus breakup does not constitute a moment of dramatic lithospheric stress drop. Instead, in-plane horizontal stress is progressively released by each main faulting episode during rifting, so that the crests of each main fault flexurally rebound, erode, and subsequently subside as deformation moves elsewhere (Figure 10 and Movies S1–S5).

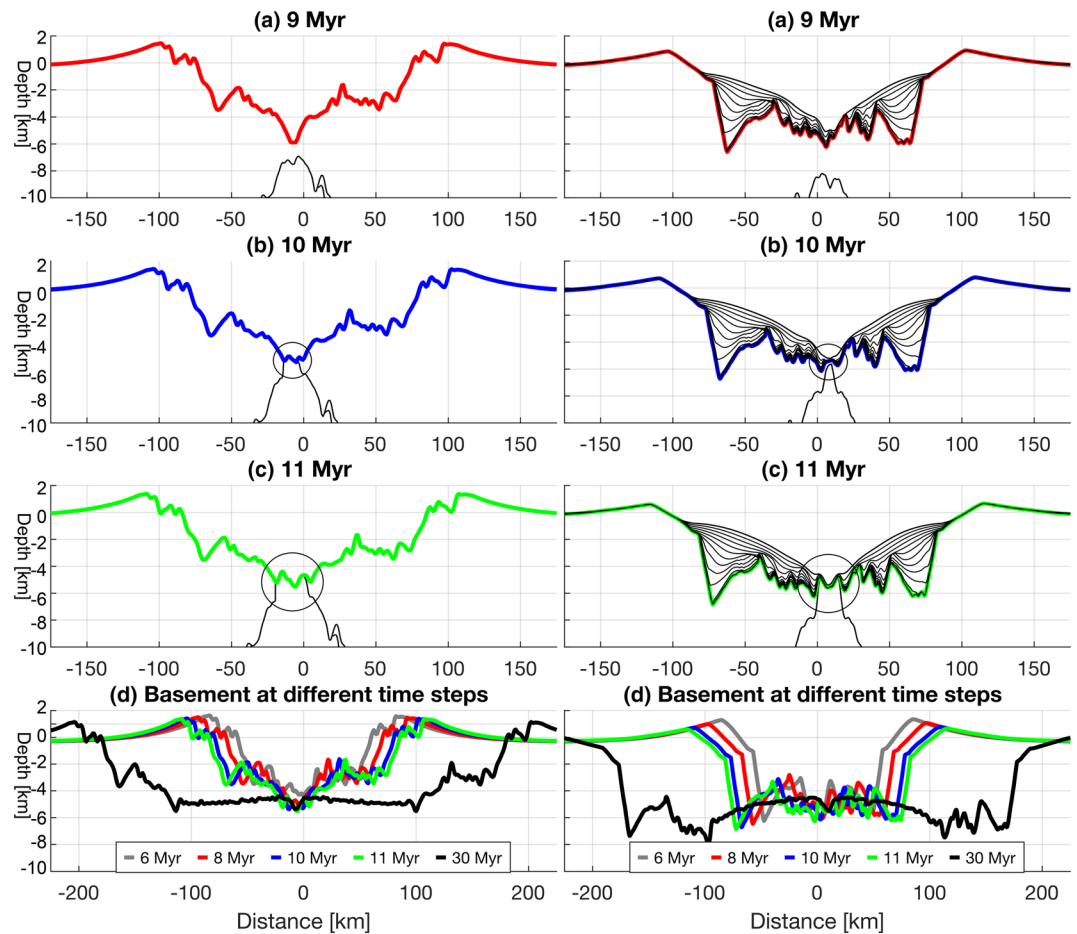


Figure 10. Basement and topography at time steps at and after breakup for Model Type 1a: narrow, strong, symmetric margins (Table 1). Panels (a)–(c) on the left hand side, show the evolution of a model with no surface processes. Panels (a)–(c) on the right hand side, show the evolution of a model with surface processes as in Figure 1a. The black circles in (b) show the breakup location, where the distal highs, shown by black circles in (c) are formed during breakup. Panels (d) show the evolution of the basement topography for different time steps during model evolution. Note the progressive rift shoulder subsidence and the relative uplift of the ocean floor at breakup and thereafter. Uplift related to breakup is laterally constrained to the distal margin areas, so that breakup does not produce a basin-wide unconformity. After breakup the model with surface processes shows more relative uplift of the ocean floor as a response to the sedimentary weight at the distal margins. This indicates that the post breakup margins and the new oceanic lithosphere continue to be mechanically welded.

Each of these episodes generates an unconformity whose overlying sediments mark the time of abandonment of fault activity over that specific area (Figures 2, 4, 6, and 8). In areas of margins where deformation consistently migrates oceanwards, these unconformities are overlain by oceanward younging posttectonic sediments, so that sediment sequences which are posttectonic in the proximal sections become syntectonic in the distal and outer margin sections. This is observed in narrow conjugate margins, in the outer sections of wide symmetric margins, and in the distal sections of the wide margin of asymmetric conjugate pairs. The narrow margin of asymmetric conjugates actively deforms throughout the rift history so that the unconformity over the whole narrow margin is approximately synchronous and coincides with breakup.

In summary, these models demonstrate that breakup of the lithosphere does not, in general, generate a basin-wide response that is recorded as a stratigraphic marker across the whole basin. This only occurs in the case of the narrow margins of asymmetric systems. Instead, the elastic stress drops associated with progressive continuous faulting and thinning generate local flexural rebounds that produce local erosive surfaces/unconformities, which mark the time of local fault activity and subsequent fault abandonment. These are here called the rift migration unconformities. When sedimentation rates are low, and/or the

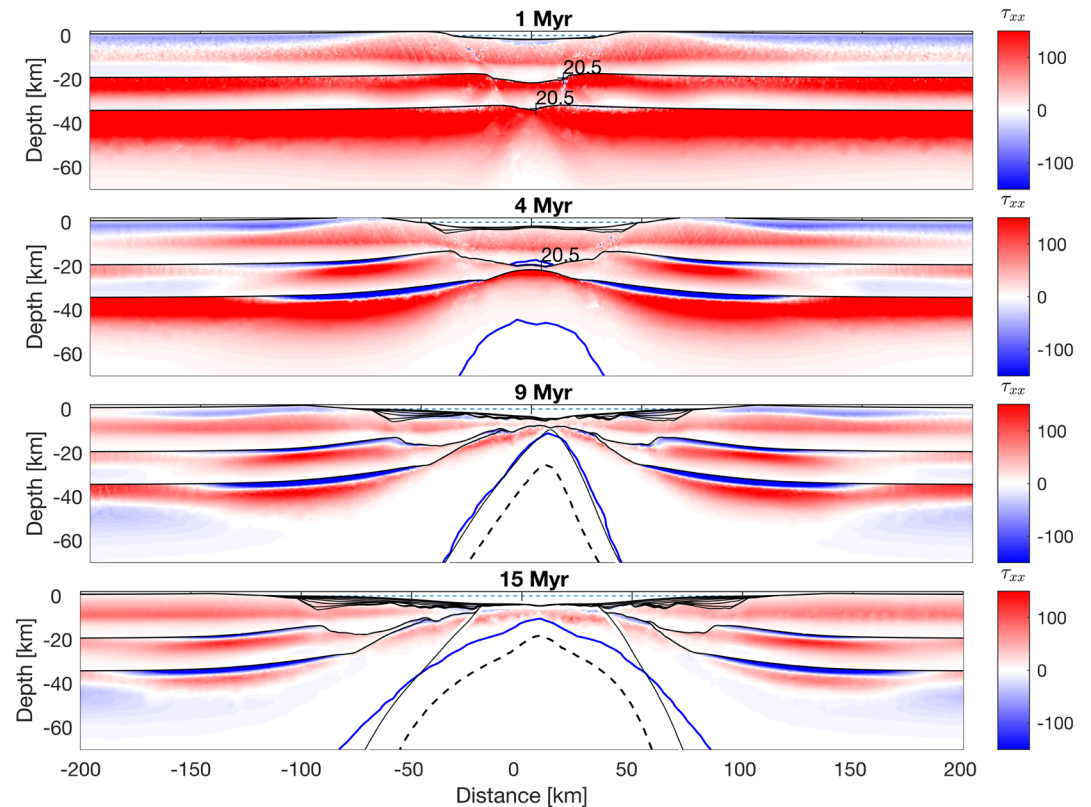


Figure 11. Horizontal stress for different time steps during the evolution of Model Type 1a (Table 1 and Figure 1a). The evolution of other models is shown in Movie S8. Dashed line shows the 1250°C isotherm, and thin black line shows the base of the continental lithosphere. Blue line shows the viscosity line for $10^{20.5}$ Pa-s. Note that the horizontal stress progressively decreases as faults cut through the strong layers. At breakup most of the horizontal stress in the crust has been released, but some still remains in the mantle. This stress is horizontally continuous and extends from the continental lithosphere beneath the distal margins to the mantle beneath the new ocean floor. Thus breakup does not constitute a moment of dramatic stress release. This continuous lateral stress decreases, and after around 20 Myr after breakup, it becomes negative in the lithospheric mantle under the distal margins (see Movie S8).

duration of rifting is relatively fast (e.g., 10 Myr or less), these unconformities may be difficult to distinguish and may appear to amalgamate in a single unconformity, often (mis)interpreted as a BU (e.g., compare Figures 4a and 4b). If the age of this unconformity is interpreted from wells in the proximal margin, then breakup will be estimated to have happened before it actually occurred.

A cautionary note to our results is that we have not modeled the formation of oceanic crust after breakup and the transient weakening related to dike injection. However, we note that we are dealing with magma-poor environments, with half-extension velocities of 5 mm yr^{-1} , where total magmatic crustal thicknesses are anticipated to be around 3 km (see Figure 4 of Ros et al., 2017). In the margins analyzed here and elsewhere a recurrent and important observation is the occurrence of distal highs (see profiles shown here and also Seismic Section 155 in the South China IODP 367–368 drilling area by Sun et al., 2019, and Nirrengarten et al., 2020, seismic profiles in southern Australia by Gillard et al., 2015, and eastern India by Pindell et al., 2014, among others). In our models these distal highs correspond to the footwalls of the last oceanward conjugate faults that breakup the crust and lead to formation of new ocean floor. The large flexural rebound experimented by these footwalls (see basement depth on markers located in the distal highs in Figures 2b, 4c, 6c, and 8b) is a reflection of the relatively high horizontal stresses at breakup (Figure 11). The morphology of these distal highs, and the onlapping of sediments on the steady uprising ocean floor, is quite similar to that observed in seismic profiles (see Figures 13–16). Hence, we suggest that in nature too, the distal highs may represent the footwalls of the last conjugate faults that lead to

breakup and that they must have broken through crust and mantle that still had some strength. Additionally, numerical models of oceanic crustal accretion through dike intrusion suggest that only at fast spreading ridges where the horizontal extension is taken up completely by magma intrusion will the horizontal stress completely drop to zero at the axis (Liu & Buck, 2020). In that case, very small oceanward and landward offset faults would form at the ridge (Liu & Buck, 2020) and would develop a morphology dissimilar to the large distal highs observed in seismic profiles and modeled here at breakup. These distal highs are more reminiscent of the median valley topography observed at slow and ultraslow spreading centers that persists through the magmatic accretion of the crust and instead imply that the ridge axis retains strength during breakup (Chen & Morgan, 1990).

4.2. Relationship Between Sedimentary and Margin Architecture: Examples From the North/South Atlantic and the South China Sea

In this section we compare our modeled margins and sedimentary architecture to natural examples of margins. The objective is to demonstrate that the above suite of models can reproduce many features seen at natural margins, so that the predicted stratigraphy can be used as a template for interpreting seismic sections (Figure 1). Our results show that the geometry, age, and spatial distribution of sedimentary packages over conjugate margin pairs varies with their tectonic architecture. In turn, their tectonic architecture can be traced back to differences in the composition of the lithosphere (LC and mantle), the initial geothermal gradient, and the way deformation initiates, that is, whether rifting is spatially localized or more widely distributed at the start of rifting (in this work this difference is modeled by the use of different initial seed techniques). In general, margins show a migration of deformation from the proximal sections toward the locus of breakup. This results in the top of the syntectonic sections, the bottom of the posttectonic sections, and the unconformities that separate these two packages not being synchronous; rather, they become younger toward the ocean. Variations to this general sedimentary pattern are related to variations in how the deformation is distributed in time and space. Here we have chosen different margins which resemble our four types of modeled margin architecture: the Porcupine basin for narrow symmetric margins, the Camamu-Gabon conjugates for rather strong asymmetric margins, the Espirito Santo-Congo margins for weak asymmetric basins, and the South China Sea for wide symmetric margins.

We note that even though we have investigated a wide range of parameters, the effect of plumes, different extension velocities, mantle rheologies, and 3-D deformation effects on sedimentary architecture has not been investigated. This will be the focus of future research.

4.2.1. Type 1a, Narrow, Symmetric Margins: The Porcupine Basin Example

The Porcupine basin is a V-shaped failed rift located in the North Atlantic, located 200 km southwest of Ireland (Figure 12; Bullois et al., 2018; Chen et al., 2018). The basin underwent significant lithospheric stretching in Mid-Late Jurassic times, with less pronounced rifting in the Permo-Triassic and Early Cretaceous (Chen et al., 2018; Tate et al., 1993). The stretching factors increase from north to south (Chen et al., 2018). The basin axis is approximately north-south, and its width increases from ~60 km in the north to ~200 km in the south where stretching factors appear to be larger than 6 (Chen et al., 2018; Prada et al., 2018). Both sides of the basin are fairly symmetric (Chen et al., 2018); thus, it can be considered a pair of narrow, symmetric margins.

We have compared our narrow, symmetric model, Type 1a (Figures 1a and 2), with a 2-D section from a recently acquired 3-D data in the western margin of the south Porcupine basin, south of Well 43/13-1 (Pedley et al., 2016). Well information here is much sparser than in the north (only three wells in the South Porcupine compared to 26 in the north, Parkinson et al., 2018; Figure 12). By the time the seismic interpretation of this area was completed, this area was virtually unexplored, with only two wells, all of them outside the 3-D seismic survey area (43/13-1 and Dunquin North, Figure 12a). The overall structure of the western margin, as observed in the seismic line, is very similar to that obtained with our Type 1a model (Figures 1a and 12). The size and depth of blocks, however, cannot be readily compared as the seismic data are presented in two-way traveltimes, TWT, and a lateral distance scale is not provided in Pedley et al. (2016). Nevertheless, these data provide one of the best published images of the syntectonic geometries of this part of the basin. The stratigraphy of the syntectonic and posttectonic sequences, within the synrift period, are quite similar between the model and seismic images. The crests of Blocks A, B, and C in both model and seismic profile are capped by an erosional unconformity. Block D is in both the seismic section and model much

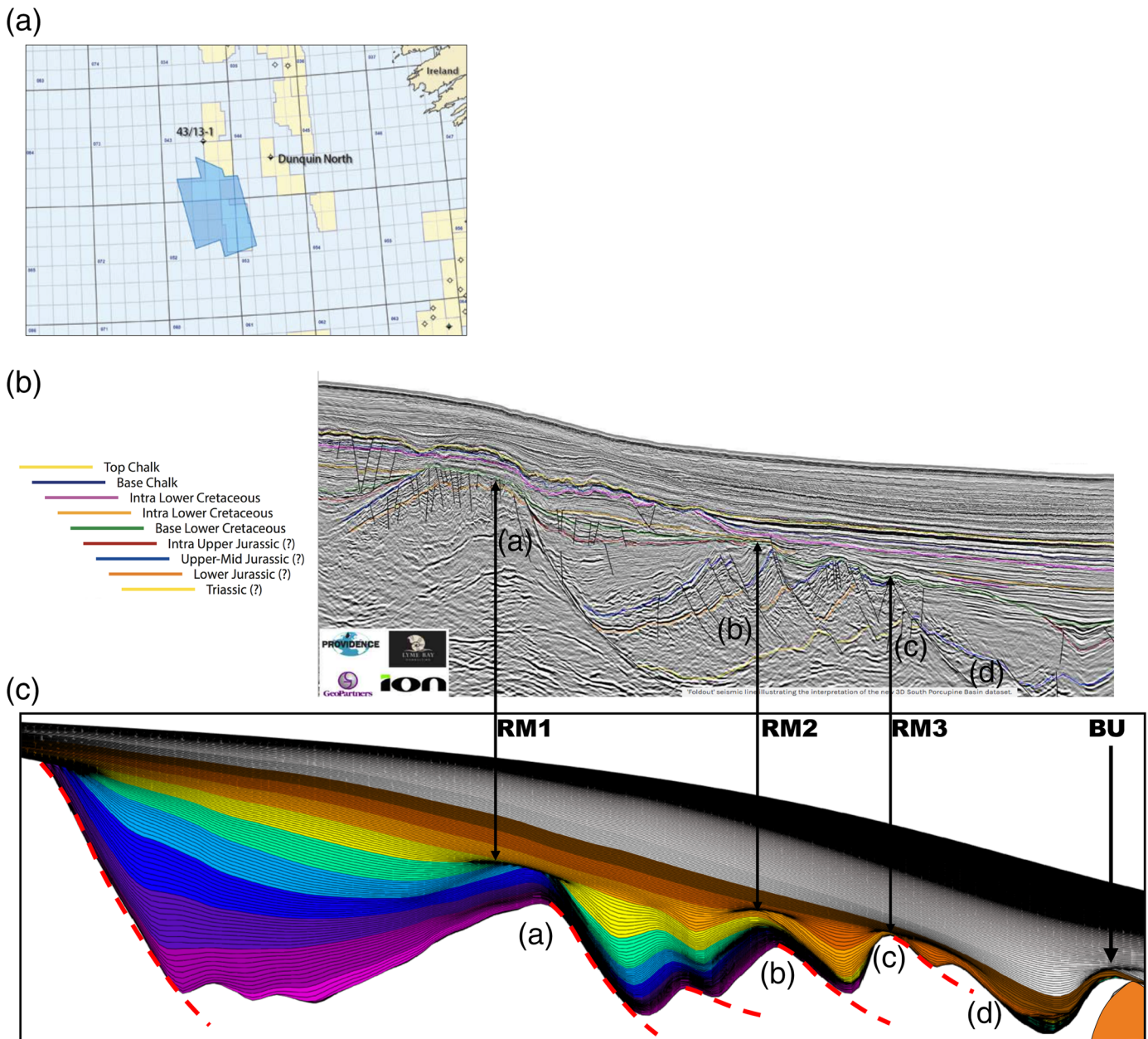


Figure 12. (a) Map showing the location of a 3-D seismic survey (blue polygon) located in the southwest Porcupine basin, from where the 2-D seismic section in (b) is extracted. (a) and (b) have been modified from Pedley et al. (2016). 43/13-1 and Dunquin North are wells in the area. (c) Zoom of Model Type 1 (Figure 1a and Table 1), at 32 Myr after rift onset. RM1, RM2, and RM3 refer to rift migration unconformities. Arrows show that similar unconformities are observed in the seismic profile. BU is the breakup unconformity in the modeled section. Red dashed lines are faults in the modeled section, and orange is the mantle. A, B, C, and D are basement blocks in both (b) and (c). Note that the interpretation of the Triassic to intra-Upper Jurassic by Pedley et al. (2016), that is, most of the synrift units, is shown with a question mark in their legend, suggesting that their interpretation is little constrained and other interpretations are possible. Dashed blue line is sea level.

deeper than the previous blocks; in our model Block D would correspond to the distal high that occurs before new ocean floor is exposed. Note that due to absence of well control in the area, the interpretation of the age of the syntectonic sequences in the seismic section is tentative (see question mark in the legend of Figure 12b). In our model, the top of the syntectonic section and the rift migration unconformities that cap it (RM1, RM2, and RM3 in Figure 12) become younger from Block A to B to C. On top of Block D the syntectonic section, shown in brown colors, thins and is uplifted seaward. In the seismic section interpretation, the top of the syntectonic section seems to be of the same age on top of Blocks A and B (red horizon) but also becomes

younger on top of Block C (green horizon). The syntectonic sequence on top of Block D in the seismic reflection image seems also to be uplifted and thin seawards (see eastern end of seismic section, between horizons red and blue); however, its top is not younger than in the blocks to the west, as shown in our model. In general, we can say that the similarity in the geometry of the basement and sediment geometry between seismic data and model points to a younging of the syntectonic section basinwards in the Porcupine that can be well described by the Type 1a: narrow, symmetric margin model described here. However, at this stage, we cannot use field data to fully confirm the results of our modeling.

4.2.2. Type 2c, Intermediate Strength Asymmetric Margins: The Camamu-Gabon Conjugates

The Camamu-Gabon margins form part of the central segment of the South Atlantic margin sector (Blaich et al., 2011; Figure 13). They constitute an asymmetric conjugate pair, where Gabon is the wide margin and Camamu the narrow one (Blaich et al., 2011; Ros et al., 2017). The width of both margins is not exactly well known as wide-angle data, and deep wells in the distal margin do not exist. The suggested width of these margins varies depending on the interpretation of the multichannel seismic data and the gravity modeling performed. For example, while in Lentini et al. (2010), the width of the hyperextended margin in Gabon (i.e., crust less than 15 km thick) is around 125 km, it is 150 km wide in Ros et al. (2017), and around the same width in Blaich et al. (2011); however, the latter authors consider the last distal 50 km of margin to host crust of transitional nature. Similarly, the thickness and extent of the Camamu basin depends on the interpretation, with thinning of the crust from 35 to breakup along ~75 km in Blaich et al. (2011) and along ~100 km in Ros et al. (2017). The difference resides again in that Blaich et al. (2011) interpret the distal part of the margin as transitional crust.

Taking these uncertainties into account, here we compare the interpreted seismic section of the Camamu-Gabon margins by Ros et al. (2017) with the results of a model with 40 km crust and an intermediate strength for the LC, that is, anorthite (Figure 13). The evolution of this model is very similar to that of mafic granulite, but we choose anorthite because it generates a wider, wide margin than does mafic granulite and a basement topography more similar to that observed in seismic sections (Figure S9 and Movie S9). The overall conjugate margin architecture, including the pattern of Moho thinning, margin width, dip, and spatial distribution of faulting, observed in the seismic section is very similar to that in the modeled section. In both model and the seismic section, the wide margin presents a depocenter in the proximal domain, where both inward and landward faults are found, followed by a central horst. In our model the depocenter is the initial proximal half-graben formed in the margin that becomes the wide one, while the central horst is the remnant of the flexural bulge formed between the two initial half-grabens (an evolution similar to Figure 5). In both the seismic section and model, the Moho thins beneath the central horst (Figure 13). Oceanward of the horst, the hyperextended crust is characterized by oceanward dipping faults in the basement and the continent-ocean boundary is marked by a subdued distal high in both the model and seismic section. In our model this area constitutes the region that experiences lateral rift migration (Figure 5). In the interpreted seismic section, the Camamu basin is narrow and thins very abruptly compared to the Gabon, a characteristic which is reproduced by the model. In the seismic section, the top of the oceanic basement just oceanwards of the distal high at the Camamu basin appears to curve upward much more than in the Gabon margin. In our model this is also the case, and it is related to the fact that the narrow margin accumulates a greater thickness of sediments over a shorter distance, so with continuing postrift loading, the oceanic basement tends to unload and bend upward more than in the wide margin. This is again a manifestation of the continuity of the horizontal stress across the margin to the oceanic plate, even after breakup.

Interpretations of the synrift stratigraphy based on wells on the platform indicate that the stratigraphy is the same in both conjugate margins with the early synrift sequences starting in the Berriasian (143 Ma) and the late synrift sequences from the early Aptian (118 Ma, Karner & Driscoll, 1999). Interpretation of seismic sections on the African side suggests that the synrift section contains an important sag sequence, which has been interpreted as an indication that rift subbasin development was diachronous with strain localization migrating oceanwards, thereby forming progressively younger depocenters toward the continental-oceanic boundary. This in turn would imply that the base of the late sag sequence is diachronous along the margin (Lentini et al., 2010). This interpretation is very well reproduced in the stratigraphy of the wide margin of the model section, where the top of the syntectonic section and the bottom of the post-tectonic section both young oceanward. The sag section in our model is approximately 2 km thick, similar to the sag thickness interpreted by Lentini et al. (2010). This sag section is found mainly over the depocenter

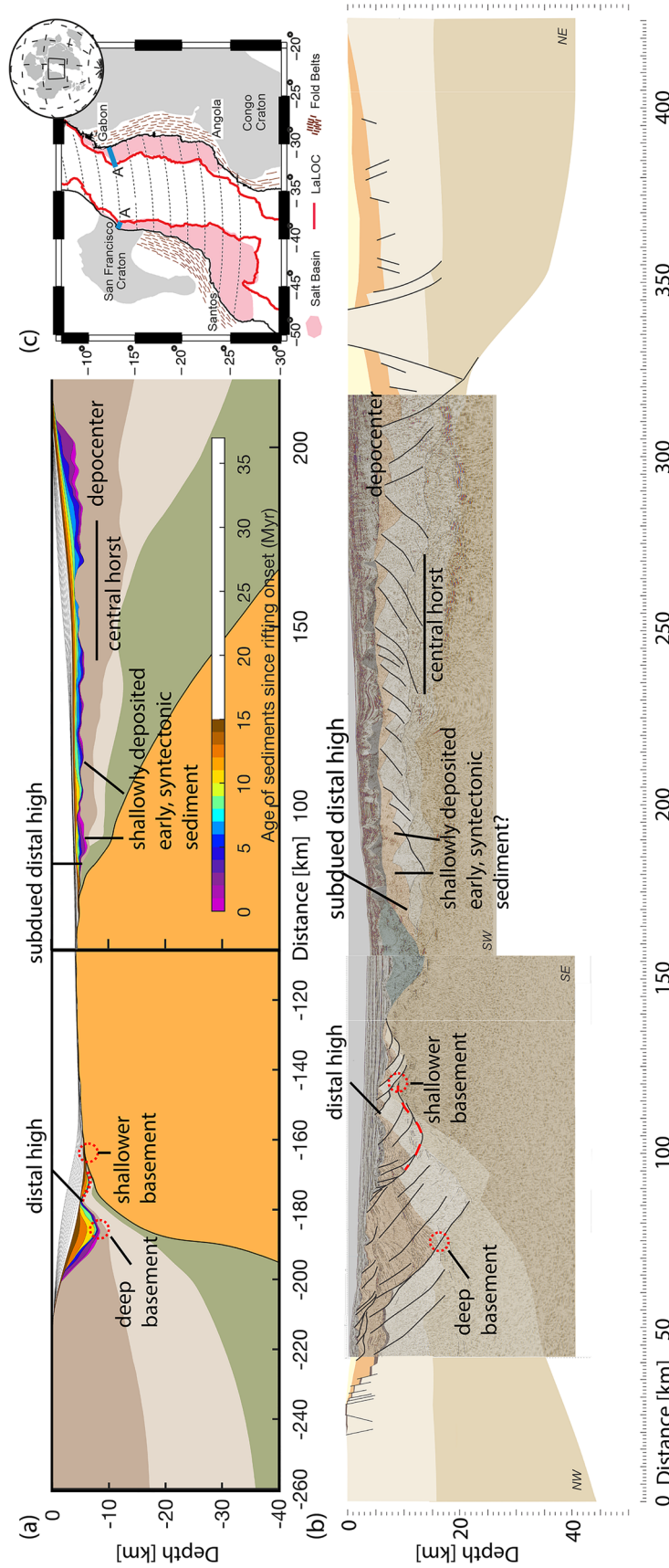


Figure 13. Comparison of (a) Model Type 2c: intermediate strength asymmetric margins (Table 1), with (b) the interpretation of the Camamu-Gabon margins by Ros et al. (2017). Panel (c) shows the location of the interpreted lines in Camamu-Gabon (map modified from Ros et al., 2017).

and central horst, and it becomes syntectonic over the outer margin in our model (yellow to brown sediments, Figure 13). In addition, the model shows that early syntectonic sediments should be found in the outer domains of the wide margin. In the model these sediments are deposited at shallow depths in the narrow margin and then transported laterally to the wide margin. Here shallow syntectonic sediments over thin crust do not imply a deficit in subsidence, as has been previously interpreted.

The Camamu basin is characterized by a very deep half-graben where thick syntectonic sediment packages accumulate. This is bounded oceanward by a distal high that appears before the first oceanic floor is exposed. These two features are well reproduced by the model, although our narrow margin is a bit narrower than the interpreted width of the Camamu basin by Ros et al. (2017) and closer to the width interpreted by Blaich et al. (2011). The synrift stratigraphy on the deep half-graben of the Camamu is not well known and is only based on wells located in the platform and on one deep well, which only penetrated late Aptian (Well 1-BAS-129, Cobbold et al., 2010). Earlier sequences of the synrift in the deep margin have yet to be characterized. If our model predictions are correct, the deep half-graben in the narrow margin should contain a bigger proportion of late to early synrift than its conjugate margin.

4.2.3. Type 2b, Weak Asymmetric Margins: Angola-Northern Campos/Espirito Santo Conjugates

These margins are located in the central part of the central segment of the South Atlantic (Blaich et al., 2011). The analyzed seismic lines are at the border between the Angola/Congo basins and the Campos/Espirito Santo basins (Figure 14d). The interpretation of the geological structures comes from multichannel seismic data (Karner & Gambôa, 2007), in addition to more modern prestack depth migrated seismic data (Lentini et al., 2010; Péron-Pinvidic et al., 2017; Unternehr et al., 2010), combined with gravity analysis (Cowie et al., 2016) and wide-angle seismic data (Moulin et al., 2005). Here we compare our Type 2b margins: weak, asymmetric margins (Figures 6 and 7), with a prestack depth migrated line acquired by GXT in the northern Campos/southern Espirito Santo basins (Unternehr et al., 2010) and the Congo Line 3 wide-angle seismic line (Leanne et al., 2016; Moulin et al., 2005; see Figures 14 and 15 for location). The seismic lines show very asymmetric margins, with a very wide margin in the African side that slowly thins from around 30 km in the platform to breakup, over a distance of 250 km (Moulin et al., 2005; Figure 15), and an abruptly thinning Brazilian side that thins over 100 km from the platform to breakup (Unternehr et al., 2010; Figure 14). Some of the most notable observations in the wide African side include (i) little brittle faulting affecting the crust, (ii) 3–4 km of the late synrift sequence over the proximal and distal margins has a sag appearance, (iii) a large salt basin overlying the sag sequence (Karner & Gambôa, 2007), and (iv) little evidence of rift shoulder uplift (Huisman & Beaumont, 2011).

Here we focus in the synrift evolution of the margins and do not enter into the question of what conditions led to large salt accumulations at the end of breakup. This may depend on the relative sea level, which in turn may have been controlled by the volcanic Walvis Ridge-Rio Grande Rise acting as a barrier to seawater from the South (Reston, 2009; Sabato Ceraldi & Green, 2016) in addition to climatic conditions at the time of rifting (Karner & Gambôa, 2007; Lentini et al., 2010). Our Type 2b model accurately reproduces most of the observations regarding the pattern of crustal thinning and synrift sedimentary architecture observed in the African side (Figure 15). In the model crustal thinning in the wide margin occurs along 300 km from the platform to the breakup point. The spatial pattern of Moho thinning in the model is very similar to the wide-angle section (Figure 15): The Moho thins abruptly in the necking domain, subsequently it thins by curving upward, then thickens again, and from that point onwards, it steadily rises oceanwards (Figures 15a and 15b). In our model the area oceanward of the necking zone where the Moho curves upward is the remainder of the central area of distributed deformation (SDD in Figures 6 and 7). This area is characterized by horsts and grabens, which cannot be seen in the interpretation of Moulin et al. (2005) but have been interpreted with the use of higher-resolution, more modern prestack depth migrated data along neighboring seismic sections (i.e., Cowie et al., 2016; Lentini et al., 2010; Sabato Ceraldi & Green, 2016; Figure 15). In the model the syntectonic sediment in this area smoothly undulates over the top basement, without clear indication of rotated synrift wedges. Here this is the byproduct of deformation dominated by ductile lower crustal flow accompanied by small offset faults. LC flows toward the areas of active faulting as the brittle layer dramatically thins over a broad area characterized by small offset faults (Movie S4 and Figure 7 from 0–20 Myr after rifting) and undulating syntectonic packages of 2–3 km of thickness (Figure 15c). In the seismic section, this sedimentation pattern has been previously attributed to detachment tectonics by Péron-Pinvidic et al. (2017) (see Figure 15d). In the model, this pattern is instead due to small offset conjugate

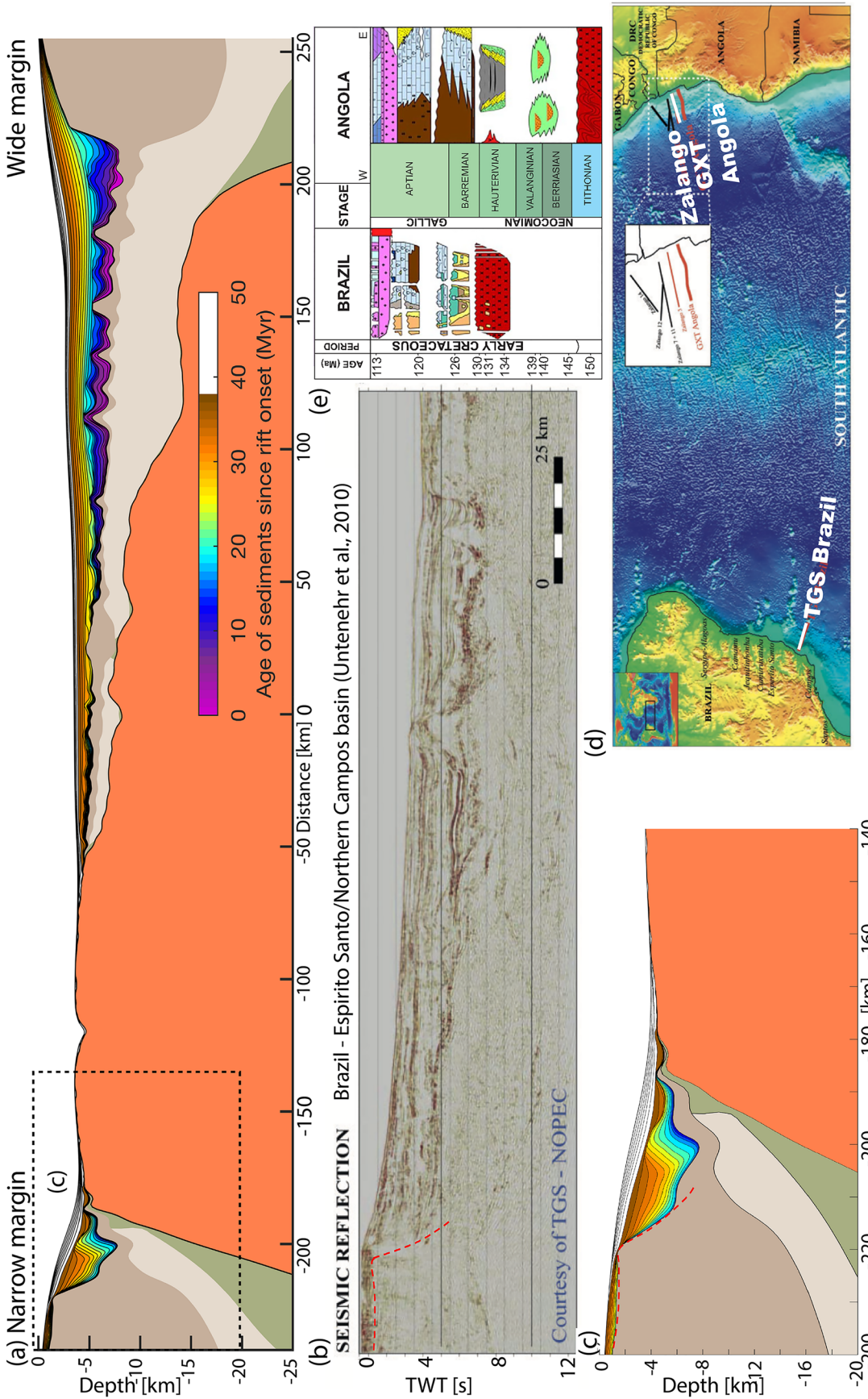


Figure 14. (a) Model Type 2b: weak, asymmetric margins, at 50 Myr after the start of rifting (see Figures 1c and 6 and Table 1). Here we compare this model to the Congo/Angola, Profile 3 of Moulin et al. (2005), in Figure 15, and to a section located in the northern Campos basin shown in (b) and reproduced from Untenehr et al. (2010). Panel (c) shows a zoom of the modeled narrow margin. Note that sections (b) and (c) are shown at the same scale. Panel (d) shows in white the locations of the seismic lines in (b) and Figure 15a used for comparison with models (reproduced from Untenehr et al., 2010). Panel (e) shows schematic stratigraphic columns for Campos and Angola (reproduced from Sabato Ceraldi & Green, 2016).

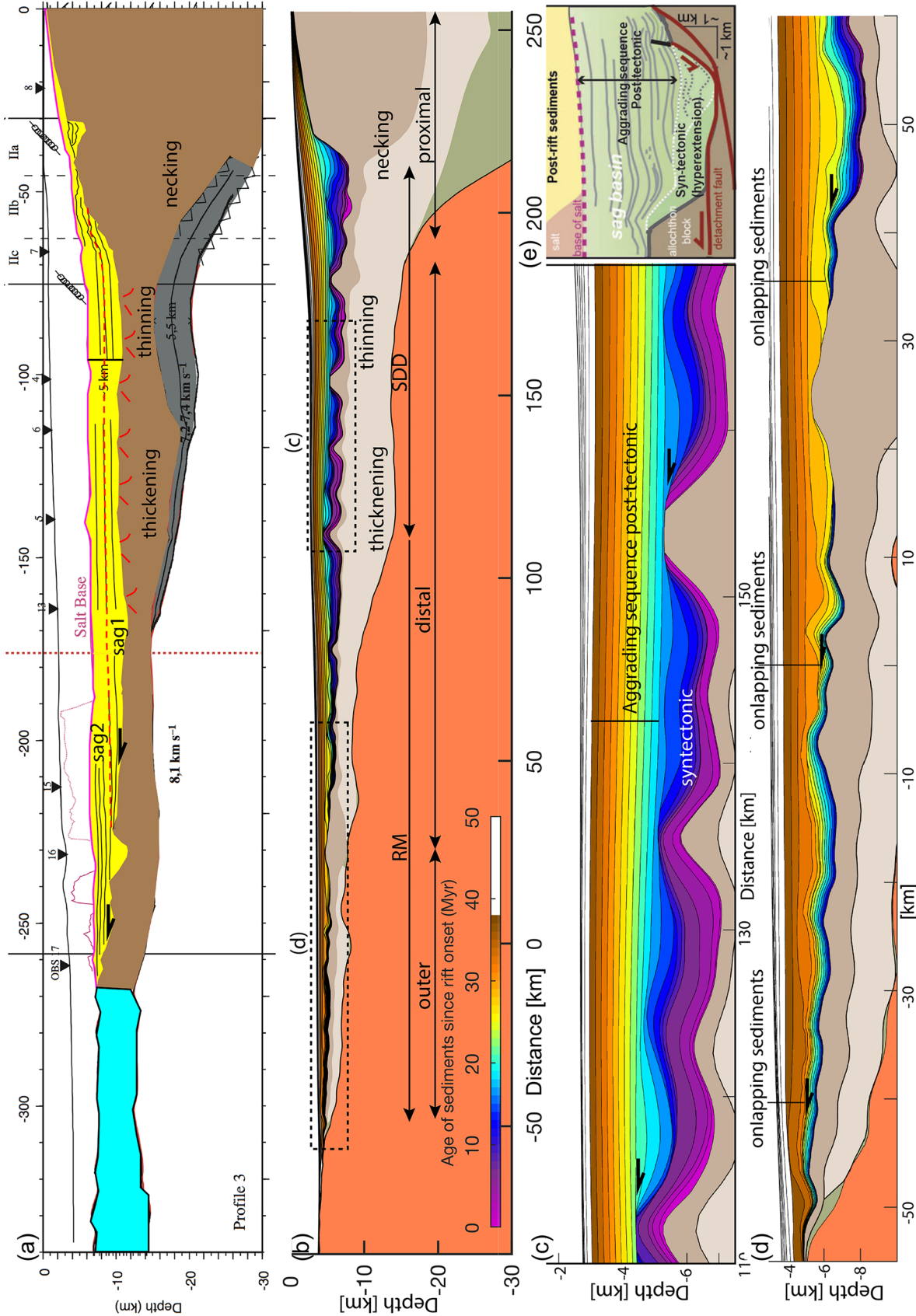


Figure 15. (a) Wide-angle profile, Congo-Zalango 3, redrawn from Moulin et al. (2005). Onlapping sediments on the distal margin are drawn following interpretations of seismic profiles from Leanne et al. (2016), Péron-Pinvidic et al. (2017), and Sabato Ceraldi and Green (2016). Red faults are schematically representing horsts and grabens interpreted by Leanne et al. (2016) and Lentini et al. (2010). Red dashed line shows the separation between Sag Sediments 1 (Sag1) and Sag Sediments 2 (Sag2) from Sabato Ceraldi and Green (2016). Panel (b) shows the wide margin of Model Type 2b: weak, asymmetric margins, at 50 Myr, at the same scale as the section in (a). SDD = area of distributed deformation; RM = area of rift migration. hi is the remnant of a horst originally located in the narrow margin. Panels (c) and (e) show close-ups of the model, and panel (d) shows a detail of a seismic section in the same area showing the geometry of the synrift sediments interpreted by Péron-Pinvidic et al. (2017).

faults on top of a very ductile and thick LC (Movie S4). The syntectonic sequence is overlain by a horizontal posttectonic synrift sequence of 2–3 km thickness. The combined thickness of the syntectonic and posttectonic sequence is around 5–6 km, similar to that of the seismic section (Figure 15).

Further oceanward in the model, the basement rises toward the breakup location, and relatively late synrift syntectonic packages onlap onto early synrift sequences (km –50 to 100 in Figures 15b, 15c, and 15e). Both these sequences appear to be subhorizontal, although they were clearly syntectonic (Movie S4). The early synrift sediments (blue colors) were originally deposited shallowly in one of the edges of the central area of distributed deformation. As deformation started to migrate laterally, they occupied a position opposite to the migration direction. With time this area and its overlying sediments were transported to the distal domains of the future wide margin. Although the geometry of the sediments may appear to result from subhorizontal detachment faulting (as interpreted from multichannel reflection seismic data), in our model, it is the result of successive small high-angle conjugate faults that migrate laterally, with faults becoming younger toward the future ocean (see Figure 7d and 25–31 Myr in model evolution Movie S4). When deformation approaches breakup, faults located in the future wide margin dominate over those in the future narrow margin (Figure 7e and 31 Myr in Movie S4). These faults result in subtle topographic highs and lows over the distal and outer domains of the margins (Figure 15c). Early syntectonic sediments are thin and pretectonic to this rift migration stage, yet appear to drape over the previous topography, as if they were posttectonic (blue sediments in Figure 15e). The syntectonic sediments to this deformation phase onlap over the pretectonic ones and appear posttectonic (yellow to orange, Figure 15c and Movie S4). Sequences similar to the blue sediment package that onlaps basement just landward of h1 (Figure 15b) may have been interpreted as Sag1 phase sediments by Sabato Ceraldi and Green (2016), while the yellow to orange sediment packages that onlap on h1 and oceanwards of it may have been interpreted as their Sag 2 sequence (see Figure 15a). If our model represents the real situation, it would predict that shallow synrift sediments deposited during early rifting in the narrow margin should be found as highly stretched subhorizontal sediments on top of the hyperextended crust of the distal and outer domains of the wide margin.

We compare the narrow margin with TGS line in the northern Campos basin from Unternehr et al. (2010) (Figure 14). Here the image beneath the salt is very poor even in prestack depth migrations, and different authors have arrived at quite different interpretations for the margin width and stratigraphic architecture (compare Sabato Ceraldi & Green, 2016; Unternehr et al., 2010). A common observation, however, is that the Brazilian side is narrower and that it has a thinner sag sequence. These two observations are reproduced in our model: a dramatically narrower margin than the African side, with syntectonic sediments exhibiting fanning toward the large bounding fault that delimits the continental platform, and a thin synrift sag sequence over the proximal half-graben, which becomes syntectonic in the outer margin (brown sequence in Figure 14c). Stratigraphic columns compiled by Sabato Ceraldi and Green (2016) show a condensed stratigraphy in the Brazilian side compared to the African side, with the earliest Berrassian to Hauterivian synrift units missing on the Brazilian side (Figure 14e). This is also predicted by our model, where it is the result of lateral transport of crust and early synrift sediments from the narrow to the wide margin (Figures 7, 14, and 15 and Movies S4 and S5).

In summary, our model suggests that the tectonic architecture of the Angola/Congo-Campos/Espirito basin conjugates is the result of thinning of lithosphere with weak LC, resulting in asymmetric margins produced by (1) an initial phase of distributed deformation, followed by (2) lateral rift migration and the cannibalization of the narrow margin. This produces a condensed stratigraphic column, with early synrift sediments missing and a thinner sag sequence in the narrow margin. The wide margin has a proximal domain characterized by horst and grabens overlain by undulating syntectonic sequences and a thicker sag sequence. Oceanwards the early syntectonic sequence from the wide margin can be found on top of hyperextended crust and is onlapped by late syntectonic sequences, which have a sag appearance. The sag sequence thickness decreases oceanwards. We infer that the whole wide margin is being tilted basinwards due to the large load from the new sediments added to the proximal margin and the extra buoyancy of the oceanic domain in comparison to the continental domain.

Our model is in agreement with interpretations that the mode of deformation in this area is related to rifting of a soft crust on a metasedimentary fold belt (Lentini et al., 2010). It also agrees with the interpretation that the sag sediments in the proximal margin are synrift but posttectonic to this area due to oceanward migration

of the deformation (Cowie et al., 2016; Lentini et al., 2010). The development of large synrift sag basins had been previously explained by Karner and Gambôa (2007) in terms of depth-dependent extension that is vertically partitioned across a zone of decoupling that resulted in the development of a relatively non-deforming UC (i.e. the upper plate: the African side) from a ductile-deforming LC and mantle (i.e. the lower plate: the Brazilian side), the boundary between them having a ramp-flat-ramp geometry. Extension of the lower plate in this scenario would then thin the lithospheric mantle and LC more than the UC. However, we find that in the proximal and distal areas of the wide margin (Figure 15b) where sag is most developed, it is the UC which thins more than the LC (Movies S4 and S5). This is the area that experienced a long period of spatially distributed deformation (SDD, Figures 6 and 7). On the other hand, the lithospheric mantle does indeed thin more than the LC and breaks before crustal breakup, as suggested by Huisman and Beaumont (2011). However, early lithospheric breakup does not imply that the weak asymmetric model would have a higher geothermal gradient than the strong one where lithospheric breakup does not predate crustal breakup. Actually, at the time of lithospheric mantle breakup in the weak, Type 2b model, 12 Myr after rift start, the 500°C isotherm is deeper than in the strong model, Type 2a, showing that the weak model is colder (Figure S10). Therefore, the lack of subsidence in the weak model compared to the strong one is not related to higher geothermal gradients due to early mantle lithosphere breakup. Instead, it is related to the existence of a very weak, thick LC, which flows toward the area of extension. This maintains a relatively thick crust and keeps a shallower depth of necking in the weak model, Type 2b, in comparison to the strong one, Type 2a.

4.2.4. Type 3: Wide Symmetric Margins: The South China Sea

The South China Sea (SCS) is a “V”-shaped basin that may have resulted from the orogenic collapse of the Cretaceous Yenshanian orogeny (Chen et al., 2010). The rift started around the Late Cretaceous/Early Paleocene and lasted for about ~30 Myr. The breakup of the major eastern subbasin of the SCS occurred in the Early Oligocene, about 32 Ma. Rifting continued and breakup in the southwest subbasin occurred in Late Oligocene, at about 25 Ma (Barckhausen & Roeser, 2004; Briais et al., 1993; Clerc et al., 2017; Franke et al., 2014). Here, we compare our modeling results for Type 3 margins to seismic profiles located at the southern tip of the oceanic propagator in the Nan Com Son and East Natuna basins (first published in Clerc et al., 2017; Franke et al., 2014; Savva et al., 2014; Figure 16). The two seismic profiles show a continental crust that slowly thins over a large lateral distance. Along profile SCS2, where breakup may have occurred, the crust thins from 8 s TWT to ~0 s TWT (~26 km to perhaps some few kilometers or 0 km) along an ~200 km lateral distance, on each margin. The basin has a total width of at least 400 km. Breakup is achieved between two relatively symmetric margins. In both seismic profiles we observe both continentward and oceanward dipping normal faults bounding horst structures and graben with classical synrift geometries. In depth sections the Moho undulates, with Moho uplifts coinciding with overlying basement grabens and downbends with basement horsts (Franke et al., 2014; Pichot et al., 2014; Savva et al., 2014). The South China Sea is also characterized by the occurrence of shallow water carbonates on top of block crests, suggestive of a delayed synrift subsidence (Franke et al., 2014).

The width of the basins, the symmetry of the conjugate margins, the existence of both landward and oceanward dipping faults, which generate a horst and graben geometry, and classical fan-wedged synrift geometries, as well as the undulations of the Moho basement following horsts and grabens in the basement in the seismics, are reproduced by Type 3 model (see Figure 16). The most notable difference between our model and the seismic data is that grabens appear to be deeper in the seismic data. This may be because the seismic sections are shown in time, and so grabens occupied by sediments, with a relatively low seismic velocity, appear deeper in seismic profiles. Actually, wide-angle data along a northern profile by Pichot et al. (2014) show that basins typically contain 4–5 km of syntectonic sediment, a thickness similar to that observed in our simulations.

Figure 8 shows the basement depth through time, at various locations from the proximal to the distal domains along the modeled section. The figure shows that the crests of blocks which are at less than 50 km from the breakup locations are at relatively shallow waters during large parts of the model evolution. For example, the yellow and orange markers sit on top of blocks that are eroded and above sea level until 5 Myr after rift onset and then at less than 1 km depth during the following 7 Myr. If these blocks were capped by synrift sediments approximately hundreds of meters in thickness, then carbonate deposition would be quite feasible during the first 5–10 Myr of rift history, as observed by Franke et al. (2014). Other block crests, located in a more landward position (gray and blue markers, ~100 km from breakup

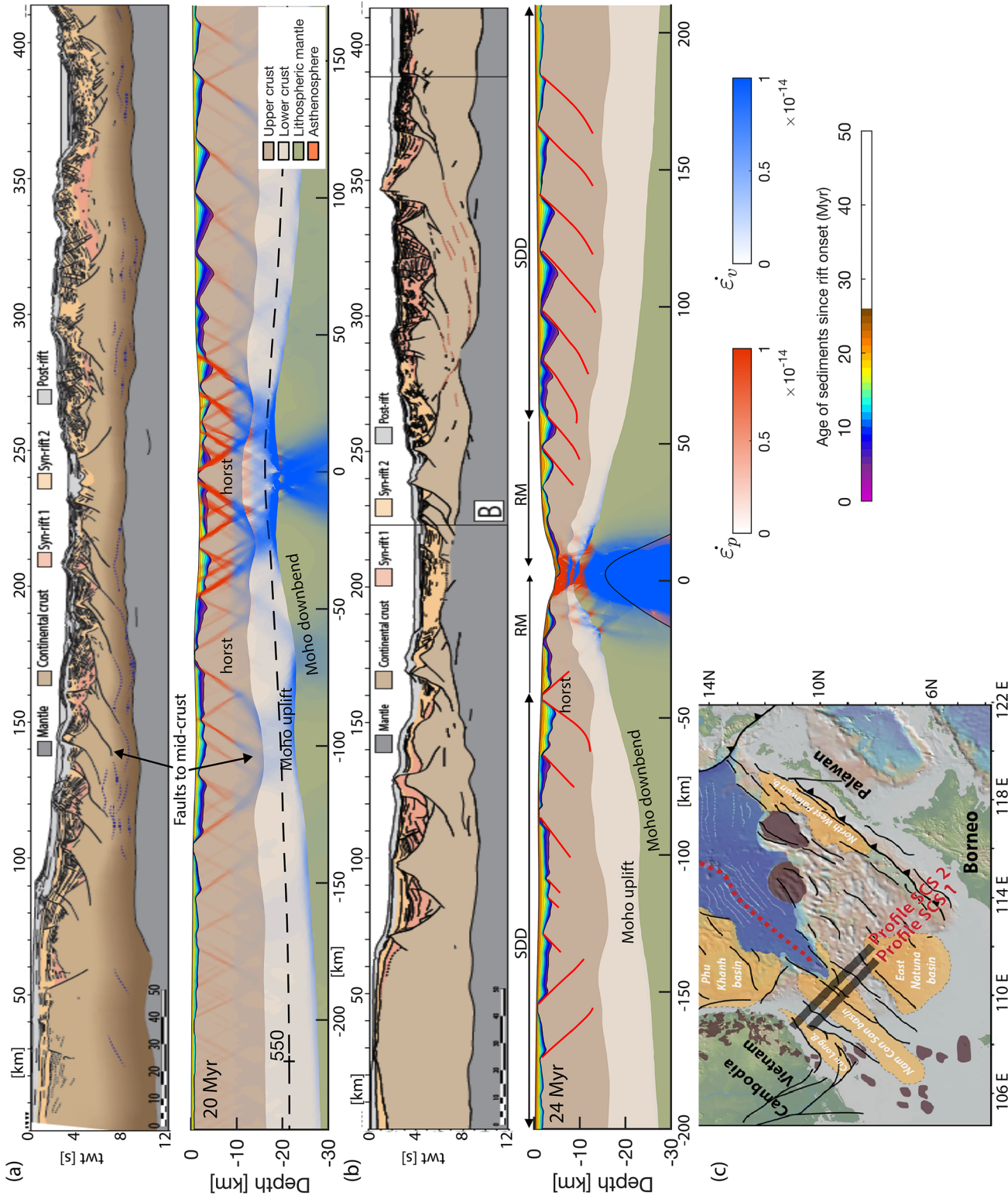


Figure 16. (a) Comparison of seismic profile SCS1 (Clerc et al., 2017), top, with the Model Type 3 at 20 Myr (Figures 1d and 8), bottom. (b) Comparison of Section SCS2 (Clerc et al., 2017), top, with the model shown in Figures 1d and 8 at 24 Myr, bottom. Note the similarity between the depth of faulting, the undulations of the Moho and the evolution of the model interpreted from seismic data (see section 4). SDD is affected by spatially distributed deformation. RM = rift migration area. (c) Map showing location of seismic lines (from Clerc et al., 2017). Red and blue shades show areas where plastic and ductile strain rate focus. Synrift sediments are shown in rainbow colors.

position, Figure 8), experience even shallower water depths. Paleobasement depths in the area of spatially distributed deformation, SDD, do not increase oceanward, but they depend on the relative time of activity of the faults bounding the blocks. The subsidence along this wide SDD area which occupies most of both margins is rather slow and appears to be delayed, as suggested by Franke et al. (2014). Only in the outermost part of the outer margin is the subsidence large, as this area thinned very rapidly in the last 5 Myr before breakup, when extension localized in a narrow area, the RM area in Figure 9, and migrated oceanwards. Note that the dark green point at the breakup location appears to uplift from 15 to 21 Myr and then rapidly subsides. Movie S6 shows that in this time period, this marker is located on top of one of the horsts that typify this type of deformation. The horst is bounded by landward dipping faults on each side and thus uplifts. After 21 Myr it is dismembered by oceanward dipping faults that lead to breakup.

The high temperatures at the Moho used in this model result in a prominent ductile behavior of the LC and importantly the mantle below the Moho. However, the fact that the compositional rheology chosen here, anorthite, is stronger than the wet quartzite used in the previous example allows for a more important role for brittle faulting that leads to the formation of clear rotational syntectonic wedges. The relatively hot LC and the RWS inhibit localization of deformation and produce a very wide area (>150 km wide on each margin) of distributed deformation during the first 20 Myr of rifting, where the Moho thins slowly, subsidence is low, and rotational syntectonic wedges are observed. Faults appear to extend into shear zones in the LC, bringing LC into their footwalls and resulting in horsts having thicker crust than grabens. This is because LC is transported from grabens toward their bounding horsts (Figure 16 and Movie S6), as observed by Franke et al. (2014), Pichot et al. (2014), and Savva et al. (2014). Localization and symmetric oceanward migration of deformation only occur over a comparatively narrow area (~50 km) and a short period of 6 Myr before breakup. In this outer domain the Moho thins and subsidence increases abruptly. Abrupt thinning over a narrow area close to the breakup margins has also been inferred from stratigraphic patterns by Cameselle et al. (2017) and wide-angle data by Pichot et al. (2014). This type of deformation is quite different from what has been described in West Iberia-Newfoundland, where the LC is probably much colder and localization of rifting, and effective crustal thinning occurred much earlier in rifting history, with asymmetric rift migration producing asymmetric conjugate margins (Ranero & Pérez-Gussinyé, 2010).

Our model predicts a synrift geometry that is remarkably different from the previous described cases. Here relatively early synrift (0–10 Myr from the start of rifting) extends over most of the proximal and distal margins and is only absent in the most outer domains, where breakup occurred. The thickness of this early synrift varies, being thicker over grabens than in horsts. Unconformities at the top of rotated blocks in the SDD do not follow a clear oceanward progression but record the random distribution of deformation during the period of wide rifting (Figure 16). Only in the outer most margins do unconformities young oceanwards, with syntectonic sediments becoming younger toward the ocean. The BU is the last local unconformity before new oceanic basement is exposed.

Our model does not reproduce the large widths observed in northern sections of the SCS where breakup occurred. Le Pourhiet et al. (2018) have suggested that those extreme widths are most likely related to 3-D effects, which we cannot model here. (They suggested that basin opening was driven by the competition between ridge propagation and compression caused by the topographic weight of the Indochina peninsula. This would generate a very wide basin ahead of the propagator.) This may well be possible; however, they could only reproduce these large widths with a weak LC rheology, which is difficult to compare to the one used here (because they used non-Newtonian rheology and had no sedimentation; see their Figure 3). Although, they suggested that 3-D effects “would erase the sensitivity of continental rifting structures to crustal rheology,” their results on the dependency of the basin width on underlying crustal rheology indicate that their statement should be softened. Most probably, the general basement and sediment morphology that we see at the small basin scale in 2-D will translate into 3-D, in the sense that different lower crustal rheologies will still give rise to different basement and sediment morphologies, as shown here. We suggest that 3-D effects are more likely to modulate the 2-D response than to erase it.

5. Conclusions and Outlook

Classical models of rifting have failed to recognize the importance of the migration of deformation, the potential for large lateral transport of sediments, and the role of the strength of the lithosphere in the sedimentary

record and the vertical movements that occur during rifting. The recognition that deformation migrates during extension and that this produces sag sequences, which are synrift, is key for understanding stratigraphic patterns (as suggested by Brune et al., 2014; Masini et al., 2013; Pérez-Gussinyé, 2013; Pérez-Gussinyé & Ranero, 2005; Péron-Pinvidic et al., 2007; Ranero & Pérez-Gussinyé, 2010, among others). Here we find that the large variety in observed stratigraphic patterns, unconformities, and their associated vertical movements depend on whether this migration is symmetric or asymmetric and on whether there is an initial phase of distributed deformation in the early stages of rifting and how long this phase lasts. We find that sedimentary architecture closely mimics rift architecture, which in turn depends on lithospheric strength and thus the nature of the terrains where rifting initiated, that is, inheritance. Figure 1 presents four of the main rift architectures analyzed here and a simplified synopsis of their stratigraphic patterns.

Narrow symmetric margins, Type 1, are formed when deformation is spatially localized from the rift onset in large conjugate faults which form the outer half-grabens and then quickly migrates symmetrically, from both conjugate sides, toward the future ocean (Figure 1a). This produces the same stratigraphic pattern on both conjugates, with the syntectonic section and the bottom of the synrift sag section younging oceanward. Consequently, rift migration unconformities are symmetric on both margins and young oceanward. The BU is the last one of these unconformities. If the LC is strong, the syntectonic geometries are more obviously rotational than when the LC is weaker.

Asymmetric margins, Type 2, form when deformation migrates laterally during rifting. Their sedimentary structure is also asymmetric, with a condensed syntectonic section in the narrow margin with respect to the wide one. In the wide margin the area of lateral rift migration is characterized by oceanward younging RM unconformities culminating in the BU, whereas in the narrow margin, there is only one unconformity, the BU, that extends over the whole margin and dates breakup. The wide margin presents a proximal area characterized by early synrift syntectonic sediment, bounded oceanwards by an area where this sediment disappears and an outer domain where relatively early synrift deposited in shallow waters overlies extremely thinned crust. This can be explained without invoking a subsidence deficit or more extension in the lower than UC (Figures 1b and 1c). This arrangement is, actually, the result of cannibalization of the basement and early synrift sediments of the narrow margin and their lateral transport to the wide margin. The length of the wide margin, its basement topography, and syntectonic geometry depend on lower crustal strength. Weak LC promotes a long period of distributed deformation in the initial phases of rifting, during which LC flows into the deforming area, resulting in more upper than lower crustal thinning and in relatively small subsidence, undulating syntectonic sediments, and large overlying sag basins that predate breakup.

Wide symmetric margins, Type 3, are characterized by a long phase of distributed deformation, ~20 Myr, that is accompanied by little subsidence, relatively small degrees of crustal thinning, and Moho uplift under grabens and downbend under horsts (Figure 1d). This culminates in a relatively sudden phase, 5–6 Myr long, of localization of deformation into a narrow area where abrupt crustal thinning, large subsidence, and breakup occurs. Here the stratigraphic pattern is symmetric and is characterized by early synrift, syntectonic sediment, which is spatially distributed over most of the length of the margin, except at the outer end of the breakup area. This sediment package is thicker in grabens and thinner in horsts where it is often eroded. Unconformities over most of the area are of similar age and only young oceanwards in the area affected by strong and sudden spatial localization leading to breakup.

Finally, breakup does not lead to a sudden decrease in horizontal stress and is only recorded in the sedimentary record as a breakup unconformity, BU, in areas affected by deformation related to the final crustal rupture. Other unconformities observed along margins, away from the breakup area, predate breakup. They record the previous migration of deformation, and we call them the rift migration unconformities, RMUs. Their spatial distribution can also be correlated to margin architecture (Figure 1). When sedimentation rate is small, or rifting is very rapid, the RMUs and the BU may appear to laterally join and can be misinterpreted as a single unconformity. Our results cannot be fully tested against data, since there are only sparse wells at continental margins and many of the distal sections of margins remain basically unexplored. However, the overall resemblance of the modeled sections to the seismic ones suggests that they can be used as templates for interpretation of the deformation mode and associated sedimentary patterns at a wide variety of margins.

Data Availability Statement

Seismic data included in this paper are available through Clerc et al. (2017), Moulin et al. (2005), Pedley et al. (2016), Péron-Pinvidic et al. (2017), Ros et al. (2017), Sabato Ceraldi and Green (2016), and Unternehr et al. (2010).

Acknowledgments

We thank Zoltán Erdős, Manuel Pubellier, and Ernst Willingshofer for their very detailed and helpful revisions that have improved this work. This work is funded by the Deutsche Forschungsgemeinschaft (DFG, German Research Foundation) under Germany's Excellence Strategy – EXC-2077 – 390741603.

References

- Andrés-Martínez, M., Pérez-Gussinyé, M., Armitage, J., & Morgan, J. (2019). Thermomechanical implications of sediment transport for the architecture and evolution of continental rifts and margins. *Tectonics*, *38*, 641–665. <https://doi.org/10.1029/2018TC005346>
- Armitage, J., Burgess, P. M., Hampson, G. H., & Allen, P. A. A. (2018). Deciphering the origin of cyclical gravel front and shoreline progradation and retrogradation in the stratigraphic record. *Basin Research*, *30*(Suppl. 1), 15–35. <https://doi.org/10.1111/bre.12203>
- Armitage, J. J., Whittaker, A. C., Zakari, M., & Campforts, B. (2018). Numerical modelling of landscape and sediment flux response to precipitation rate change. *Earth Surface Dynamics*, *6*, 77–99. <https://doi.org/10.5194/esurf-6-77-2018>
- Barckhausen, U., & Roeser, H. A. (2004). Seafloor spreading anomalies in the South China Sea revisited. In P. Clift, W. Kuhnt, P. Wang, & D. E. Hayes (Eds.), *Continent-ocean interactions in the East Asian Marginal Seas, Geophysical Monograph Series* (Vol. 149, pp. 121–125). American Geophysical Union. <https://doi.org/10.1029/149GM07>
- Blaich, O. A., Faleide, J. I., & Tsikalas, F. (2011). Crustal breakup and continent-ocean transition at South Atlantic conjugate margins. *Journal of Geophysical Research*, *116*, B01402. <https://doi.org/10.1029/2010JB007686>
- Braun, J., & Beaumont, C. (1989). A physical explanation of the relation between flank uplifts and the breakup unconformity at rifted continental margins. *Geology*, *17*(8), 760–764. [https://doi.org/10.1130/0091-7613\(1989\)017<0760:APEOTR>2.3.CO;2](https://doi.org/10.1130/0091-7613(1989)017<0760:APEOTR>2.3.CO;2)
- Briaais, A., Patriat, P., & Tapponnier, P. (1993). Updated interpretation of magnetic anomalies and sea floor spreading stages in the South China Sea: Implications for the Tertiary tectonics of Southeast Asia. *Journal of Geophysical Research*, *98*(B4), 6299–6328. <https://doi.org/10.1029/92JB02280>
- Brun, J.-P. (1999). Narrow rifts versus wide rifts: Inferences for the mechanics of rifting from laboratory experiments. *Philosophical Transactions of the Royal Society A: Mathematical Physical and Engineering Sciences*, *357*(1753), 695–712. <https://doi.org/10.1098/rsta.1999.0349>
- Brun, J.-P., & Beslier, M. O. (1996). Mantle exhumation at passive. *Earth and Planetary Science Letters*, *142*(1–2), 161–173. [https://doi.org/10.1016/0012-821x\(96\)00080-5](https://doi.org/10.1016/0012-821x(96)00080-5)
- Brune, S., Heine, C., Clift, P. D., & Pérez-Gussinyé, M. (2017). Rifted margin architecture and crustal rheology: Reviewing Iberia–Newfoundland, central South Atlantic, and South China Sea. *Marine and Petroleum Geology*, *79*, 257–281. <https://doi.org/10.1016/j.marpetgeo.2016.10.018>
- Brune, S., Heine, C., Pérez-Gussinyé, M., & Sobolev, S. V. (2014). Rift migration explains continental margin asymmetry and crustal hyperextension. *Nature Communications*, *5*, 4014. <https://doi.org/10.1038/ncomms5014>
- Buck, W. R. (1991). Modes of continental lithospheric extension. *Journal of Geophysical Research*, *96*(B12)(20), 20,161–20,178. <https://doi.org/10.1029/91JB014851991>
- Bullock, C., Pubellier, M., Chamot-Rooke, N., & Wartremez, L. (2018). From orogenic collapse to rifting: A case of the northern Porcupine Basin: Offshore Ireland. *Journal of Structural Geology*, *114*, 139–162. <https://doi.org/10.1016/j.jsg.2018.06.021>
- Cameselle, A. L., Ranero, C. R., Franke, D., & Barckhausen, U. (2017). The continent-ocean transition on the northwestern South China Sea. *Basin Research*, *29*, 73–95. <https://doi.org/10.1111/bre.12137>
- Chen, C., Watremez, L., Prada, M., Minshull, T. A., Edwards, R. A., O'Reilly, B. M., et al. (2018). From continental hyperextension to seafloor spreading: New insights on the Porcupine Basin from wide-angle seismic data. *Journal of Geophysical Research: Solid Earth*, *123*, 8312–8330. <https://doi.org/10.1029/2018JB016375>
- Chen, Y., & Morgan, W. J. (1990). A nonlinear rheology model for mid-ocean ridge axis topography. *Journal of Geophysical Research*, *95*, 17583. <https://doi.org/10.1029/JB095iB11p17583>
- Chen, Y., Niu, F., Liu, R., Huang, Z., Tkal, H., Sun, L., & Chan, W. (2010). Crustal structure beneath China from receiver function analysis. *Journal of Geophysical Research*, *115*, B03307. <https://doi.org/10.1029/2009JB006386>
- Chenin, P., Manatschal, G., Decarlis, A., Schmalholz, S., Duret, T., & Beltrando, M. (2019). Emersion of distal domains in advanced stages of continental rifting explained by asynchronous crust and mantle necking. *Geochemistry, Geophysics, Geosystems*, *20*, 3821–3840. <https://doi.org/10.1029/2019GC008357>
- Clerc, C., Ringenbach, J. C., Jolivet, L., & Ballard, J. F. (2017). Rifted margins: Ductile deformation, boudinage, continentward-dipping normal faults and the role of the weak lower crust. *Gondwana Research*, *53*, 20–40. <https://doi.org/10.1016/j.gr.2017.04.030>
- Cobbold, P. R., Gilchrist, G., Scotchman, I., Chioffi, D., Chaves, F., Gomes de Souza, F., & Lilletveit, R. (2010). Large submarine slides on a steep continental margin (Camamu Basin, NE Brazil). *Journal of the Geological Society, London*, *167*(3), 583–592. <https://doi.org/10.1144/0016-76492009-033>
- Cochran, J. R. (1983). Effects of finite extension times on the development of sedimentary basins. *Earth and Planetary Science Letters*, *66*, 289–302. [https://doi.org/10.1016/0012-821X\(83\)90142-5](https://doi.org/10.1016/0012-821X(83)90142-5)
- Contrucci, I., Matias, L., Moulin, M., Géli, L., Klingelhofer, F., Nouzé, H., et al. (2004). Deep structure of the West African continental margin, between 5°S and 8°S, from reflection/refraction seismics and gravity data. *Geophysical Journal International*, *158*(2), 529–553. <https://doi.org/10.1111/j.1365-246X.2004.02303.x>
- Couzens, C. (1992). The rift to drift transition and sequence stratigraphy at passive continental margins, PhD Thesis. Univ. of Liverpool.
- Cowie, L., Angelo, R. M., Kuszniir, N., Manatschal, G., & Horn, B. (2016). Structure of the ocean–continent transition, location of the continent–ocean boundary and magmatic type of the northern Angolan margin from integrated quantitative analysis of deep seismic reflection and gravity anomaly data. In T. Sabato Ceraldi, R. A. Hodgkinson, G. Backe (Eds.), *Petroleum geoscience of the West Africa margin*, Geological Society, London, Special Publications (Vol. 438, pp. 159–176). <https://doi.org/10.1144/SP438.6>
- Cowie, P. A., Underhill, J. R., Behn, M. D., Lin, J., & Gill, C. E. (2005). Spatio-temporal evolution of strain accumulation derived from multi-scale observations of Late Jurassic rifting in the northern North Sea: A critical test of models for lithospheric extension. *Earth and Planetary Science Letters*, *234*(3–4), 401–419. <https://doi.org/10.1016/j.epsl.2005.01.039>

- Cunha, T. (2008). Gravity anomalies, flexure and the thermo-mechanical evolution of the West Iberia Margin and its conjugate of Newfoundland [PhD thesis]. University of Oxford.
- Dabrowski, M., Krotkiewski, M., & Schmid, D. W. (2008). MILAMIN: MATLAB-based finite element method solver for large problems. *Geochemistry, Geophysics, Geosystems*, 9, Q04030. <https://doi.org/10.1029/2007GC001719>
- Dick, H., Jian, J., & Schouten, H. (2003). An ultraslow-spreading class of ocean ridge. *Nature*, 426(6965), 405–412. <https://doi.org/10.1038/nature02128>
- Driscoll, N. W., Hogg, J. R., Christie-Blick, N., & Karner, G. D. (1995). Extensional tectonics in the Jeanne d'Arc Basin, offshore Newfoundland: Implications for the timing of break-up between Grand Banks and Iberia. *Geological Society, London, Special Publications*, 90(1), 1–28. <https://doi.org/10.1144/GSL.SP.1995.090.01.01>
- Driscoll, N. W., & Karner, G. D. (1998). Lower crustal extension across the northern Carnarvon basin, Australia: Evidence for an eastward dipping detachment. *Journal of Geophysical Research*, 103(B3), 4975–4991. <https://doi.org/10.1029/97JB03295>
- Embry, A. F., & Dixon, J. (1990). The breakup unconformity of the Amerasia Basin, Arctic Ocean: Evidence from Arctic Canada. *Geological Society of America Bulletin*, 102(11), 1526–1534. [https://doi.org/10.1130/0016-7606\(1990\)102<1526:TBUOTA>2.3.CO;2](https://doi.org/10.1130/0016-7606(1990)102<1526:TBUOTA>2.3.CO;2)
- Esedo, R., van Wijk, J., Coblenz, D., Meyer, R., Wijk, J. V., Coblenz, D., & Meyer, R. (2012). Uplift prior to continental breakup: Indication for removal of mantle lithosphere. *Geosphere*, 8(5), 1078–1085. <https://doi.org/10.1130/GES00748.1>
- Falvey, D. A. (1974). The development of continental margins in plate tectonic theory. *Australian Journal of Petroleum Exploration*, 14, 95–106. <https://doi.org/10.1071/aj73012>
- Franke, D., Savva, D., Pubellier, M., Steuer, S., Mouly, B., Auxietre, J.-L., et al. (2014). The final rifting evolution in the South China Sea. *Marine and Petroleum Geology*, 58, 704–720. <https://doi.org/10.1016/j.marpetgeo.2013.11.020>
- Gawthorpe, R. L., Jackson, C. A.-L., Young, M. J., Sharp, I. R., Moustafa, A. R., & Leppard, C. W. (2003). Normal fault growth, displacement localization and the evolution of normal fault populations: The Hamman Farauq fault block, Suez rift, Egypt. *Journal of Structural Geology*, 25(8), 1347–1348. [https://doi.org/10.1016/S0191-8141\(03\)00059-2](https://doi.org/10.1016/S0191-8141(03)00059-2)
- Gillard, M., Autin, J., Manatschal, G., Sauter, D., Munschy, M., & Schaming, M. (2015). Tectonomagmatic evolution of the final stages of rifting along the deep conjugate Australian-Antarctic magma-poor rifted margins: Constraints from seismic observations. *Tectonics*, 34, 753–783. <https://doi.org/10.1002/2015TC003850>
- Hirth, G., & Kohlstedt, D. (2003). Rheology of the upper mantle and the mantle wedge: A view from the experimentalists. In G. Hirth & D. Kohlstedt (Eds.), *Inside the subduction factory* (pp. 83–105). Washington, DC: American Geophysical Union. <https://doi.org/10.1029/138GM06>
- Huisman, R., & Beaumont, C. (2011). Depth-dependent extension, two-stage breakup and cratonic underplating at rifted margins. *Nature*, 473(7345), 74–78. <https://doi.org/10.1038/nature09988>
- Karner, G. D., & Driscoll, N. W. (1999). Tectonic and stratigraphic development of the West African and eastern Brazilian margins; insights from quantitative basin modeling. *Geological Society, London, Special Publications*, 153(1), 11–40. <https://doi.org/10.1144/GSL.SP.1999.153.01.02>
- Karner, G. D., & Gambôa, L. A. P. (2007). Timing and origin of the South Atlantic pre-salt sag basins and their capping evaporites. *Geological Society, London, Special Publications*, 285(1), 15–35. <https://doi.org/10.1144/SP285.2>
- Kaufman, P., Grotzinger, J. P., & McCormick, D. S. (1991). Depth-dependent diffusion algorithm for simulation of sedimentation in shallow marine depositional systems. *Bulletin—Kansas Geological Survey*, 233, 489–508.
- Keen, C. E. (1985). The dynamics of rifting: Deformation of the lithosphere by active and passive driving forces. *Geophysical Journal International*, 80, 95–120. <https://doi.org/10.1111/j.1365-246x.1985.tb05080.x>
- Le Pourhiet, L., Chamot-Rooke, N., Delescluse, M., May, D. A., Watremez, L., & Pubellier, M. (2018). Continental break-up of the South China Sea stalled by far-field compression. *Nature Geoscience*, 11, 605–609. <https://doi.org/10.1038/s41561-018-0178-5>
- Lentini, M., Fraser, S. C., Sumner, S., & Davies, R. J. (2010). Geodynamics of the central South Atlantic conjugate margins: Implications for hydrocarbon potential. *Petroleum Geoscience*, 16(3), 217–229. <https://doi.org/10.1144/1354-079309-909>
- Lescoutre, R., Tugend, J., Brune, S., Masini, E., & Manatschal, G. (2019). Thermal evolution of asymmetric hyperextended magma-poor rift systems: Results from numerical modeling and Pyrenean field observations. *Geochemistry, Geophysics, Geosystems*, 20, <https://doi.org/10.1029/2019GC008600>
- Liu, Z., & Buck, W. R. (2020). Global trends of axial relief and faulting at plate spreading centers imply discrete magmatic events. *Journal of Geophysical Research: Solid Earth*, 125, e2020JB019465. <https://doi.org/10.1029/2020JB019465>
- Masini, E., Manatschal, M., & Mohn, G. (2013). The Alpine Tethys rifted margins: Reconciling old and new ideas to understand the stratigraphic architecture of magma-poor rifted margins. *Sedimentology*, 60, 174–196. <https://doi.org/10.1111/sed.12017>
- Mattei, M., D'Agostino, N., Zanani, I., Kondopoulou, D., Pavlides, S., & Spatharas, V. (2004). Tectonic evolution of fault-bounded continental blocks: Comparison of paleomagnetic and GPS data in the Corinth and Megara basins (Greece). *Journal of Geophysical Research*, 109, B02106. <https://doi.org/10.1029/2003JB002506>
- McKenzie, D. (1978). Some remarks on the development of sedimentary basins. *Earth and Planetary Science Letters*, 40(1), 25–32. [https://doi.org/10.1016/0012-821X\(78\)90071-7](https://doi.org/10.1016/0012-821X(78)90071-7)
- Moulin, M., Aslanian, D., Olivet, J. L., Contrucci, I., Matias, L., Géli, L., et al. (2005). Geological constraints on the evolution of the Angolan margin based on reflection and refraction seismic data (ZaiAngo project). *Geophysical Journal International*, 162(3), 793–810. <https://doi.org/10.1111/j.1365-246X.2005.02668.x>
- Naliboff, J. B., Buitert, S. J. H., Péron-Pinvidic, G., Osmundsen, P. T., & Tetreault, J. (2017). Complex fault interaction controls continental rifting. *Nature Communications*, 8, 1179. <https://doi.org/10.1038/s41467-017-00904-x>
- Nestola, Y., Storti, F., & Cavozi, C. (2015). Strain rate-dependent lithosphere rifting and necking architectures in analog experiments. *Journal of Geophysical Research: Solid Earth*, 120, 584–594. <https://doi.org/10.1002/2014JB011623>
- Nirrengarten, M., Mohn, G., Kusznir, N. J., Sapin, F., Despinos, F., Pubellier, M., et al. (2020). Different expressions of rifting on the South China Sea margins. *Marine and Petroleum Geology*, 58, 579–598. <https://doi.org/10.1016/j.marpetgeo.2014.05.023>
- Parkinson, N., Thomas, R., & Mackay, H. (2018). Prospectivity of Ireland's Porcupine Basin, *GeoExPro* (Vol. 15, No. 5). <https://www.geoexpro.com/articles/2018/10/prospectivity-of-ireland-s-porcupine-basin>
- Pedley, T., Spear, G., & Byrne, K. (2016). Ireland: South Porcupine Basin, *GeoExPro* (Vol. 12, No. 3–2016).
- Pérez-Gussinyé, M. (2013). A tectonic model for hyperextension at magma-poor rifted margins: An example from the West Iberia–Newfoundland conjugate margins. *Geological Society, London, Special Publications*, 369, 403–427. <https://doi.org/10.1144/SP369.19>
- Pérez-Gussinyé, M., & Ranero, C. (2005). On the relationship between crustal thinning, faulting and asymmetry development during rifting. *Geophys. Res. Abstracts*.

- Pérez-Gussinyé, M., Reston, T. J., & Morgan, J. P. (2001). Serpentinization and magmatism during extension at non-volcanic margins: The effect of initial lithospheric structure. *Geological Society, London, Special Publications*, 187(1), 551–576. <https://doi.org/10.1144/gsl.sp.2001.187.01.27>
- Péron-Pinvidic, G., Mantaschal, M., Massini, E., Sutra, E., Flament, J.-M., Hauptert, I., & Unternehr, P. (2017). Unravelling the along-strike variability of the Angola–Gabon rifted margin: A mapping approach. *Geological Society, London, Special Publications*, 438, 49–76. <https://doi.org/10.1144/SP438.1>
- Péron-Pinvidic, G., Manatschal, G., Minshull, T. A., & Sawyer, D. S. (2007). Tectonosedimentary evolution of the deep Iberia–Newfoundland margins: Evidence for a complex breakup history. *Tectonics*, 26, TC2011. <https://doi.org/10.1029/2006TC001970>
- Pichot, T., Delescluse, M., Chamot-Rooke, N., Pubellier, M., Qiu, Y., Meresse, F., et al. (2014). Deep crustal structure of the conjugate margins of the SW South China Sea from wide-angle refraction seismic data. *Marine and Petroleum Geology*, 58, 627–643. <https://doi.org/10.1016/j.marpetgeo.2013.10.008>
- Pindell, J., Graham, R., & Horn, B. (2014). Rapid outer marginal collapse at the rift to drift transition of passive margin evolution, with a Gulf of Mexico case study. *Basin Research*, 26, 1–25. <https://doi.org/10.1111/bre.12059>
- Prada, M., Lavoué, F., Mudasar Saqab, M., O'Reilly, B. M., Lebedev, S., Walsh, J. J., & Childs, C. (2018). Across-axis variations in petro-physical properties of the North Porcupine Basin, offshore Ireland: New insights from long-streamer traveltimes tomography. *Basin Research*, 31, 59–76.
- Ranero, C. R., & Pérez-Gussinyé, M. (2010). Sequential faulting explains the asymmetry and extension discrepancy of conjugate margins. *Nature*, 468(7321), 294–299. <https://doi.org/10.1038/nature09520>
- Reeve, M. T. (2017). The structural and stratigraphic expression of continental breakup. PhD Thesis, Imperial College.
- Reston, T. J. (2009). The extension discrepancy and synrift subsidence deficit at rifted margins. *Petroleum Geoscience*, 15(3), 217–237. <https://doi.org/10.1144/1354-079309-845>
- Ros, E., Pérez-Gussinyé, M., Aarújo, M., Thoaldo Romeiro, M., Andres-Martinez, M., & Morgan, J. P. (2017). Lower crustal strength controls on melting and serpentinisation at magma-poor margins: Potential implications for the South Atlantic. *Geochemistry, Geophysics, Geosystems*, 18, 4538–4557. <https://doi.org/10.1002/2017GC007212>
- Royden, L., & Keen, C. E. (1980). Rifting processes and thermal evolution of the continental margin of eastern Canada determined from subsidence curves. *Earth and Planetary Science Letters*, 51(2), 343–361. [https://doi.org/10.1016/0012-821X\(80\)90216-2](https://doi.org/10.1016/0012-821X(80)90216-2)
- Sabato Ceraldi, T., & Green, D. (2016). Evolution of the South Atlantic lacustrine deposits in response to Early Cretaceous rifting, subsidence and lake hydrology. *Geological Society, London, Special Publications*, 438, 77–98. <https://doi.org/10.1144/SP438.10>
- Savva, D., Pubellier, M., Franke, D., Chamot-Rooke, N., Meresse, F., Steuer, S., & Auxietre, J. L. (2014). Different expressions of rifting on the South China Sea margins. *Marine and Petroleum Geology*, 58, 579–598. <https://doi.org/10.1016/j.marpetgeo.2014.05.023>
- Smith, T. R., & Bretherton, F. P. (1972). Stability and the conservation of mass in drainage basin evolution. *Water Resources Research*, 8(6), 1506–1529. <https://doi.org/10.1029/WR008i006p01506>
- Soares, D. M., Alves, T. M., & Terrinha, P. (2012). The breakup sequence and associated lithospheric breakup surface: Their significance in the context of rifted continental margins (West Iberia and Newfoundland margins, North Atlantic). *Earth and Planetary Science Letters*, 355–356, 311–326. <https://doi.org/10.1016/j.epsl.2012.08.036>
- Sun, Z., Lin, J., Qiu, N., Jian, Z., Wang, P., Pang, X., et al. (2019). The role of magmatism in the thinning and breakup of the South China Sea continental margin. *National Science Review*, 6, 871–876. <https://doi.org/10.1093/nsr/nwz116>
- Svartman Dias, A. E., Lavier, L. L., & Hayman, N. W. (2015). Conjugate rifted margins width and asymmetry: The interplay between lithospheric strength and thermomechanical processes. *Journal of Geophysical Research: Solid Earth*, 120, 8672–8700. <https://doi.org/10.1002/2015JB012074>
- Tate, M. P., White, N., & Conroy, J. J. (1993). Lithospheric extension and magmatism in the Porcupine Basin, west of Ireland. *Journal of Geophysical Research*, 98(B8), 13,905–13,923. <https://doi.org/10.1029/93JB00890>
- Tetreault, J., & Buitert, S. (2018). The influence of extension rate and crustal rheology on the evolution of passive margins from rifting to break-up. *Tectonophysics*, 746, 155–172. <https://doi.org/10.1016/j.tecto.2017.08.029>
- Tucholke, B. E., Sawyer, D. S., & Sibuet, J. C. (2007). Breakup of the Newfoundland–Iberia rift. In G. D. Karner, G. Manatschal, L. M. Pinheiro (Eds.), *Imaging, mapping and modelling continental lithosphere extension and breakup* (Vol. 282, pp. 9–46). Geological Society, London, Special Publications. <https://doi.org/10.1144/sp282.1>
- Unternehr, P., Peron-Pinvidic, G., Manatschal, G., & Sutra, E. (2010). Hyper-extended crust in the South Atlantic: In search for a model. *Petroleum Geoscience*, 16(3), 207–215. <http://doi.org/10.1144/1354079309-904>
- Walsh, J. J., Childs, C., Imber, J., Manzocchi, T., Watterson, J., & Nell, P. A. R. (2003). Strain localization and population changes during fault system growth within the Inner Moray Firth, Northern North Sea. *Journal of Structural Geology*, 25(2), 307–315. [https://doi.org/10.1016/S0191-8141\(02\)00028-7](https://doi.org/10.1016/S0191-8141(02)00028-7)
- Weissel, J. K., & Karner, G. D. (1989). Flexural uplift of rift flanks due to mechanical unloading of the lithosphere during extension. *Journal of Geophysical Research*, B10, 13,919–13,950. <https://doi.org/10.1029/jb094ib10p13919>

References From the Supporting Information

- Armitage, J. J., Allen, P. A., Burgess, P. M., Hampson, G. J., Whittaker, A. C., Duller, R. A., & Michael, N. A. (2015). Sediment transport model for the Eocene Escanilla sediment-routing system: Implications for the uniqueness of sequence stratigraphic architectures. *Journal of Sedimentary Research*, 85(12), 1510–1524. <https://doi.org/10.2110/jsr.2015.97>
- Armitage, J., Duller, R., & Schmalholz, S. (2014). The influence of long-wavelength tilting and climatic change on sediment accumulation. *Lithosphere*, 6(5), 303–318. <https://doi.org/10.1130/L343.1>
- Gleason, G. C., & Tullis, J. (1995). A flow law for dislocation creep of quartz aggregates determined with the molten salt cell. *Tectonophysics*, 274(1), 1–23. [https://doi.org/10.1016/0040-1951\(95\)00011-B](https://doi.org/10.1016/0040-1951(95)00011-B)
- Huffman, G., Adler, R., Bolvin, D., & Gu, G. (2009). Improving the global precipitation record: GPCP version 2.1. *Geophysical Research Letters*, 36(L17808). <https://doi.org/10.1029/2009GL040000>
- Schutt, D., & Leshner, C. (2006). Effects of melt depletion on the density and seismic velocity of garnet and spinel lherzolite. *Journal of Geophysical Research*, 111, B05401. <https://doi.org/10.1029/2003JB002950>
- Turcotte, D., & Schubert, G. (2002). *Geodynamics*. Cambridge: Cambridge University Press.
- Wilks, K., & Carter, N. (1990). Rheology of some continental lower crustal rocks. *Tectonophysics*, 182(1–2), 57–77.